A bonded Discrete Element Method for modeling ship-ice interactions in broken and unbroken sea ice fields

Oriol Jou[1], Miguel Angel Celigueta[1,2], Salvador Latorre[1], Ferrán Arrufat[1] and Eugenio Oñate[1,2]

[1] Centre Internacional de Metodes Numerics a l'Enginyeria (CIMNE), Barcelona, Spain
[2] Universitat Politècnica de Catalunya (UPC), Barcelona, Spain

Abstract

This work investigates the failure patterns of ice cakes and floe-ice when loaded by a moving and sloping structure (ice-breaking ships and cones).
In the paper we introduce the most frequently encountered ice-infested scenarios, the main characteristics of ice-breaking ships and the predicted failure modes of floe-ice depending on the loading conditions, the structure type and the ice feature dimensions and thickness.
For the simulations, a local bonded Discrete Element Method (DEM) is used to model sea ice and its fractures. The packing of bonded spherical particles which reproduce the ice continuum can break due to ship-ice interactions and the failure modes are studied.
A set of validation simulations are first carried out. A level ice sheet breaking against an installed ice-breaking cone with different slope angles is studied and the results are compared with other DEM simulations. Then, a group of bonded DEM simulations are performed to predict the different failure modes produced when an ice-breaking ship bow contacts with ice cakes and floe-ice of different dimensions and thickness, typical in broken ice fields. Finally, the study of breaking a continuous level ice sheet is carried out by modeling with the bonded DEM an "infinite" large domain of sea ice and loaded by a Single Degree of Freedom model of an ice-breaking ship.

Keywords: Discrete Element Method (DEM), bonded DEM, level ice, floe-ice, ice fractures, ice-breaking ship-ice interactions

1 Introduction

Because global warming is speeding up the melting of polar regions, navigation through ice-infested areas is becoming more frequent [19]. Therewith, new maritime routes are being opened, which were impractical a few years ago, allowing new commercial opportunities to energy companies engaged in oil and gas exploration and production, as well as for the companies which build and produce ice-breaking vessels and ice-going ships [16]. As [18] and [14] stated, investigation on the ice loads exerted on ice-navigation ships and offshore structures in contact with ice environments is a key part of polar and Arctic activities, and it is also important in ship design. Proof of that is the significant difference that characterizes the shape and structural strength of an ice-breaking vessel versus standard vessels.

Ice modeling and simulation is not as straightforward as other engineering materials. Ice in its natural and unspoiled state appears in different areas on Earth, mainly at the top of the most important mountain ranges and in the north and southern regions. Ice can be present either as

freshwater or saline ice, formed from pure or salty water, respectively. Furthermore, it can be on land or floating in the ocean. There is an increasing need to deal with ice environments in order to perform diverse working activities.

Conversely to other materials, ice has been less scarcely studied, even if in the last decades many advances have been made. In addition, it is a complicated material to characterize. Firstly, because of the large number of variables that influence its formation and growth, secondly due to its complex chemical composition and heterogeneity (when saline formed by solid ice, solid salts, brine and gas), and finally for its multiple types and forms possible to appear [41]. For this and much more, the study of ice has been and continues to be a great challenge.

Focusing on sea ice, it can be classified by several criteria; age, feature type, position in relation to land and open sea, forms of floating type, etc. [23]. Regarding age, if sea ice has not more than one winter's growth it is called first-year (FY) ice and its thickness may range between 0.3 m to 2.0 m [41]. The micro-structure of such ice is formed by four different layers with different properties. They are, from sea surface to the ice sheet bottom: Primary ice (P), Transition zone, Secondary ice (S) or columnar zone and Tertiary ice (T) [22]. This type of sea ice can be split into different categories depending on the crystals orientation from the columnar zone: S2 for random horizontal orientation of c-axis and S3 for preferred aligned orientation of c-axis. For engineering applications the FY-S2 ice is the most studied one because the major portion of first-year ice floes consist of such columnar ice. Also the ice covers in the Arctic form through unidirectional solidification in the direction of the heat flow, and are comprised of columnar-shaped grains whose crystallographic c-axis tend to lie within the plane of the sheet, introducing the anisotropic behavior with cross isotropy [38]. Additionally, because the c-axis is randomly oriented within that plane in most locations of the Arctic Ocean, the S2 ice type is the most probable one to appear.

From an engineering point of view, understanding the mechanical behavior of sea ice is necessary in order to model it accurately. In general, sea ice exhibits two kind of inelastic behaviors. On one hand, when slowly loaded it flows plastically (creep phenomenon). On the other hand, ice fractures when it is rapidly loaded [36]. This behavior trend is described by the ductile-to-brittle transition with the stress-strain curve evolving from low to high strain rates when loaded by uniaxial compression. At low strain rates (ductile regime), ice behaves plastically with post-peak softening. Increases in strain rate within this regime leads to peak failure followed by softening. At critical strain rates near and above the transition one, the stress-strain relations become brittle. Hence, a nearly linear ascending branch with abrupt failure is observed [37]. Most, the ship-ice and structure-ice interactions are within the brittle range. For this reason an elasto-brittle model will be considered for the simulations carried out in this work.

Sea ice waters are complex environments to define because there are multiple types of ice present; level ice, deformed ice, rafted ice, ice ridges, hummocks, etc. [23]. Despite this complexity, roughly two type of ice fields can be described: broken and unbroken. An iced sea with the presence of ice can both be formed by a continuous ice platform (level ice) or by a discontinuous plane of clearly differentiate blocks and floes of ice with minimal or null confinement between each other. The study of this configuration is not treated in this work and requires a separate study.

An ice sheet may fail in several modes: crushing, bending, buckling, splitting, spalling or creeping [11]. The failure mode is determined by the following variables; ice feature, structure definition and interaction details. This topic is discussed further in the following section. In general, when interacting with conical structures, ice covers fail in bending mode. In contrast, when interacting with vertical structures, ice covers fail in crushing mode [13].

The numerical tools available today are useful to reproduce and digitally simulate possible scenarios where ice can be both applicant and requested actor. Some numerical methods have been used for analysis of structure-ice interaction problems. In this paper the Discrete Element

Method (DEM) is used due to its proven capacity to model multiple fractures in brittle materials [21,31,35]. The DEM has been applied to the simulation of pancake floe-ice [39] and rubble pile accumulation against inclined structures [32]. The DEM has been extensively used as a numerical technique for reproducing the behavior of granular materials (discontinuum media) with good results. In recent years the DEM has been extended to the analysis of continuum media (the so-called bonded DEM). Intense research has been carried out on multi-fracture and failure of solids involving geomaterials and concrete [2]. Even more recently, the DEM has been used for modelling the mechanical behavior of ice, considered as a frictional material [25]. A promising line of research is the combined finite-discrete element approach to model ice sheet from the transition of continuous media to fractured and separated pieces [33].

This paper examines the usefulness of a particular local bonded DEM [31] for structure-ice and ship-ice interactions. The ice sheet failure against a narrow structure is firstly studied and the results compared with other DEM models. Secondly, the failure of ice features are studied both for broken and unbroken ice environments loaded by a moving ice-breaking vessel. As mentioned earlier, ice is treated as an elastic-brittle material and it is shown that ice failure is dependent on the ice conditions, the structure shape and the interaction details between the ice feature and the structure.

The paper starts with a brief analysis of the main characteristics of the ice-breaking ships and especially the problem that occurs when navigating in frozen seas. For broken ice fields a detailed analysis of the types of fractures that occur in an ice floe when it is loaded by an ice-breaking ship is described. According to the thickness and dimensions of the ice floe, a theoretical failure mode is defined. A bonded DEM formulation for modeling the mechanics of ice and its fracture is detailed. The interaction of a packed group of discrete particles allows to model an ice sheet and study the possible fractures and their propagation. Buoyancy effects on the floating or submerged ice particles are taken into account in all the problems studied in this work. Finally a set of numerical simulations of ice fracture are carried out. In the first group, we present how a continuous sheet of level ice breaks against an installed cone in a vertical structure. The influence of the slope of the cone is studied both in the type of breakage and for the magnitude of the ice loads. In the second group of simulations, a detailed study of the types of fracture produced in finite size ice floes is presented, varying their thickness and sizes. These are understood as isolated elements of a discontinuous sea of ice formed by separated blocks, the confinement of which is very small or null. The influence of thickness and dimensions of the ice floes on ice loads is studied. Finally, we present a simulation of the advance of a 3D model of a real ice-breaking vessel through an unbroken ice field composed of 1.0 meter thick FY level ice. The results are compared with those expected and observed in real navigation and the forces generated are used to estimate the required propulsion power.

2 Ice-breaking vessels performance in ice-infested waters

The interaction between a structure and an ice floe is a problem composed of several phenomena. The more relevant ones are: breaking, rotation, sliding and clearing or rubble formation. The occurrence of each one depends on the type and geometry of the structure. Vertical and sloping water line structures are used but the interaction process with ice is different. A sloping structure used for ice-breaking purposes induces lower ice forces than those caused by the ice failure in a bending mode [12]. Ice-breaking vessels are characterized by a flat shape bow, defined by a low buttock angle at the stem in order to take advantage of the bending failure pattern and the reduced forces. The sketches in Figure 1 highlight the difference in the bow between an icebreaker vessel and a standard vessel.

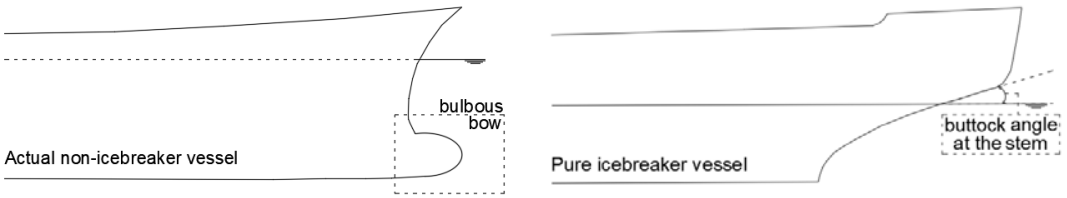

(a) Standard vessel. (b) Icebreaker vessel.

Figure 1: Longitudinal sketches of vessels.

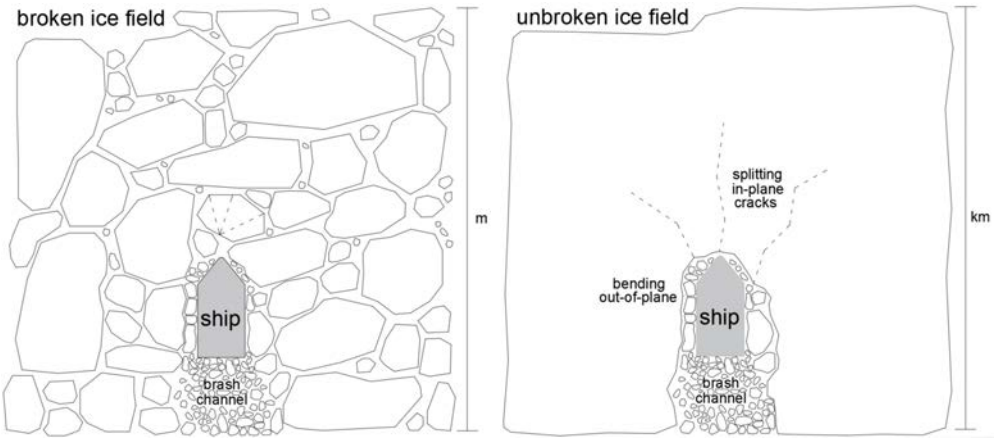

(a) Sketch of a ship navigating through a broken ice field made of finite size ice floes. (b) Sketch of a ship navigating through an unbroken ice field composed of level ice.

Figure 2: Drawings of the two most frequently encountered scenarios in ship-ice interactions.

2.1 Definition of ice fields

Ice-breaking vessels navigating through frozen seas and structures can encounter different ice features. From that, two different scenarios are described: broken and unbroken ice fields. Figure 2a shows a sketch of a ship navigating through *a broken ice field* made of different size ice floes. This situation is typical during the melting season, along late spring and summer, if ice lasts. The ice blocks have arbitrary shapes and usually their contacts are weak enough to be considered as separated pieces. That is the reason why the study of this type of situations is done by isolating a single ice floe. The possible types of failure of an ice floe are introduced in the following section. Figure 2b shows a sketch of a ship navigating through an *unbroken ice field* characterized by a continuous sheet of huge dimensions (from hundred meters to kilometers) formed by, ideally, level ice. Focusing on ice-breaking vessels, when they advance through a continuous and vast level ice sheet two failure modes are likely to appear around the ship and in its local vicinity: the crushing and the flexural modes. Depending on the ice conditions, the ship can generate large linear cracks that travel along the ice sheet opening a lead starting at the ship's bow. Even so, they are more difficult to appear when confinement of ice is present in the field.

2.2 Overview of isolated floe-ice fractures

Several Arctic expeditions reported that usually during winter and early spring months FY sea ice forms a relatively large and uniform ice field. Thus, the ice-breaking vessel primarily travels producing only local failure modes, mainly crushing and bending. When the conditions permit it

and relatively small ice floes or ice floes with little confinement are present, the splitting failure tends to appear. Therefore, the local failures are alleviated and the ice-breaking ship travels within the lead created. Several material and interaction variables are considered to affect the fracture processes. They are summarized in **ice feature aspects**: floe size, ice thickness, ice concentration, ice confinement and material strength, and **interaction description**: interaction speed and contact properties. We will study their influence in the simulations carried out.

Considering the need to identify and classify the failure modes of single ice floes, we consider different scenarios depending on the mentioned variables. The following assumptions are taken into account:

- An open and broken ice field is assumed and, subsequently, only the failure of a single ice floe is studied.
- A finite size ice floe is idealized as resting on the sea surface. Hence, only contact buoyancy and gravitational forces act on it.
- A rectangular geometric shape is assumed because ice floes exhibit in winter a rectangular shape, while in summer they are more rounded.
- For simplicity and numerical model requirements, the ice material is assumed to be homogeneous, isotropic and elastic-brittle.

The failure scenarios of isolated ice cakes and small ice floes are classified according to a criteria based on the dimensions (L and B) and the characteristic length (l) of the ice plate [29]. A sufficiently small ice cake can be directly rotated by the action of the vertical force component before any relevant fracture occurs. If the ice floe size increases, flexural failure becomes inevitable and it is influenced by the free boundaries. At this moment the ice floe fractures by creating radial cracks from the loading point to the free opposed borders. These cracks are first controlled by crack initiation followed by crack propagation.

The characteristic lengths of cracks vary with the considered ice thickness and are calculated as [27,29]:

$$l = \sqrt[4]{\frac{D}{k}} = \sqrt[4]{\frac{Eh_i^3}{12\left(1-\nu^2\right)\rho_w g}} \tag{1}$$

D is defined as the flexural rigidity of the ice plate and its expression depends as the Young's modulus (E) and the Poisson's ratio (ν) of ice and the plate thickness (h_i) as:

$$D = \frac{Eh_i^3}{12\left(1-\nu^2\right)} \tag{2}$$

where k is the so-called foundation modulus. It is defined in terms of the sea water density (ρ_w) and the gravitational acceleration (g) as:

$$k = \rho_w g \tag{3}$$

Depending on the ice-floe dimensions, compared with the characteristic length (l), results in the classification of which scenarios will present flexural failure. In [24,26–29] there is a detailed explanation of specific mathematical models to describe all these ice behaviors. For our interest, only the classification is studied in order to see if the DEM approach is suitable to reproduce good simulations.

Knowing the ice floe dimensions (L and B), the thickness (h_i) and the characteristic length of the plate (l), and considering a rectangular-shape ice floe, the expected failure scenarios for an isolated ice floe are:

- Direct ice cake rotation, L $< l$
- Radial cracking of a finite size wide ice floe, $l \leq$ L $\leq 2l$
- Radial and transverse cracking of a finite size square ice floe, $l \leq$ L $\leq 2l$
- Transverse cracking of a finite size long ice floe, $l \leq$ B $\leq 2l$
- Radial and circumferential cracking of a semi-infinite ice floe L $> 2l$

Summarizing, the type of failure mode that will appear depends mainly on the shape of the sloping structure interacting with ice and the dimensions and confinement of the ice floe. Figure 3 shows some sketches of all the possible situations, with or without fracture, that may appear when an ice-breaking ship contacts with an ice floe of specific dimensions and with null confinement at the boundaries.

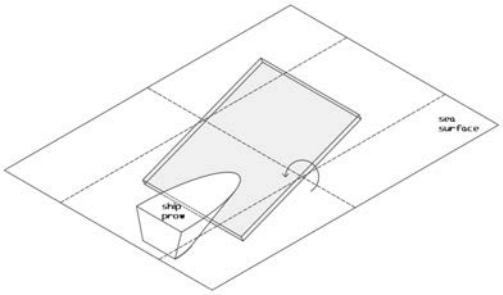

(a) Direct ice cake rotation, L $< l$.

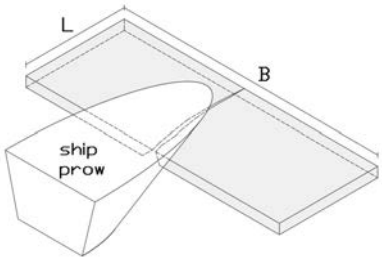

(b) Radial cracking of a finite size wide ice floe, $l \leq$ L $\leq 2l$.

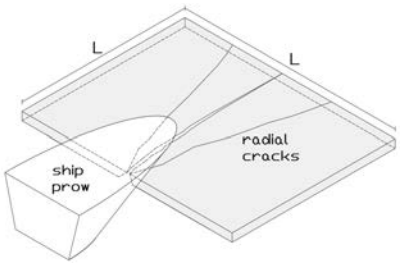

(c) Radial cracking of a finite size square ice floe, $l \leq$ L $\leq 2l$.

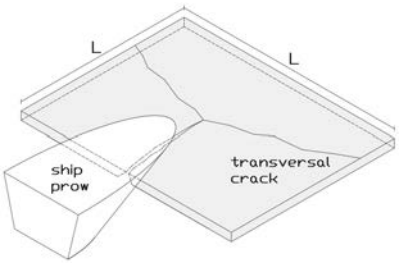

(d) Transverse cracking of a finite size square ice floe, $l \leq$ L $\leq 2l$.

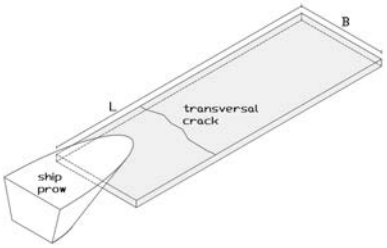

(e) Transverse cracking of a finite size long ice floe, $l \leq$ B $\leq 2l$.

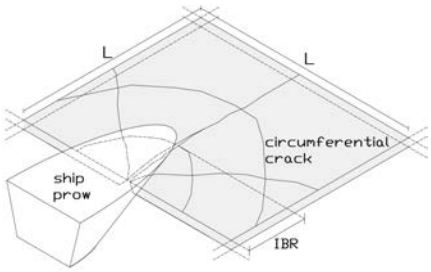

(f) Radial and circumferential cracking of a semi-infinite ice floe L $> 2l$.

Figure 3: Sketches of the possible failure modes of isolated ice floes of different dimensions when compacted by an ice-breaking vessel.

2.3 Main specifications of ice-breaking vessels

The ice-breaking vessels specifications required to carry out numerical simulations to capture the interaction of a ship with floe-ice are mainly: bow shape and buttock angle at the stem, navigation speed in ice fields and propulsion power.

For the bow shape we will focus on the part below the water line, which is characterized by the buttock angle, forming a slope. The propulsion power will be a reference value when checking the required power generated by the forces when trying to fracture ice. This computation will allow us to estimate if an icebreaker has the sufficient power to break ice and navigate in an efficient way. Finally, the navigation speed in ice fields is limited and depends mainly on the ice thickness. Table 1 gives reference ranges for the aforementioned variables.

Buttock angle	**Propulsion power**	**Ice navigation speed**
15 - 30	7.500 - 60.000	1 - 15
degrees	kW	knots

Table 1: General icebreaker vessel specifications [1,6,9,40,43].

3 Bonded Discrete Element Method for ice modeling

The local bonded DEM formulation presented herein has been implemented in the DEMPack code (`www.cimne.com/dempack/`). DEMPack has been developed at CIMNE within Kratos Multiphysics (`http://www.cimne.com/kratos/`), an Open-Source software framework for the development of numerical methods for solving multidisciplinary engineering problems.

3.1 General DEM framework

The DEM was initially developed by Cundall et al. [4] in the 1970's. It is based in the interaction of discrete elements (also called particles) – typically cylinders (in 2D) and spheres (in 3D) – to simulate the behavior of continuum and discontinuum domains [3,7,8,10,20,21,31,34,35,42]. This interaction is governed by a set of dynamic equilibrium equations involving the displacements, the velocities and the accelerations of the particles induced by the forces acting on the discrete element. The forces acting over a discrete element are related to the stresses and strains according to a constitutive model. In our work we use the local constitutive model for cohesive (bonded) and non-cohesive materials for DEM analysis proposed by Oñate et al. [31]. In the following sections a brief description of this model is presented. An enhanced non-local version of the bonded constitutive model is presented in [3].

3.1.1 Kinematic equations and integration scheme

The translation and rotation of the particles in the DEM is governed by the standard dynamics equations for rigid bodies,

$$m_i \ddot{\mathbf{u}}_i = \mathbf{F}_i \qquad , \qquad \mathbf{I}_i \dot{\boldsymbol{\omega}}_i = \mathbf{T}_i \tag{4}$$

where $\mathbf{u}_i$ and $\boldsymbol{\omega}_i$ are the displacement vector and the angular velocity vector of the i-th particle respectively, m_i and $\mathbf{I}_i$ are the mass and the inertia tensor of the particle, and $\mathbf{F}_i$ and $\mathbf{T}_i$ are vectors containing the forces and torques due to the interaction of a particle with its neighbors (Figure 4). The set of forces applied on a particle include external forces ($\mathbf{F}_i^{ext}$), damping forces ($\mathbf{F}_i^{damp}$) and interaction forces between neighbor particles ($\mathbf{F}^{ij}$) (Figure 5)

$$\mathbf{F}_i = \mathbf{F}_i^{ext} + \mathbf{F}_i^{damp} + \sum_{j=1}^{n_i} \mathbf{F}^{ij} \tag{5}$$

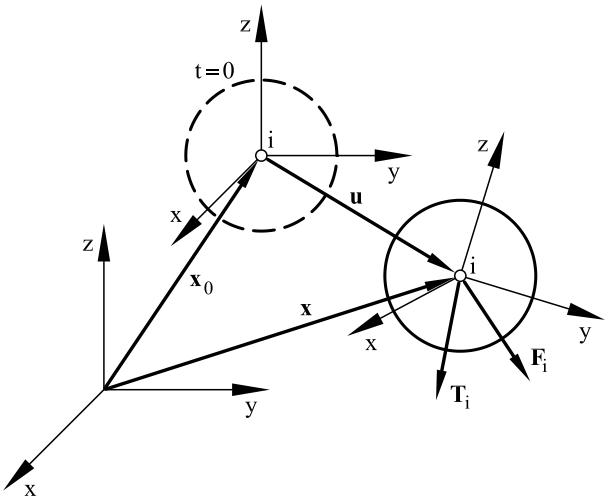

Figure 4: Motion of a rigid particle

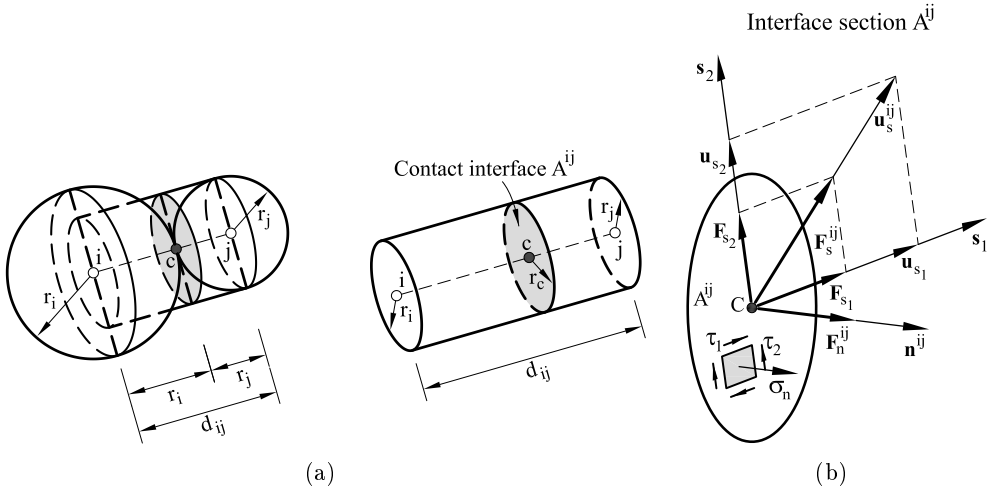

Figure 5: (a) Definition of contact interface between two discrete particles. (b) Forces acting along the normal and shear directions on a contact interface section A^{ij}

220 where n is the number of particles adjacent to the ith particle.

The expression for the torques can be derived from Eq. (5) [30]. The dynamic equations (4) are integrated in time using an explicit scheme as expressed in (6) for the translation motion

$$\ddot{\mathbf{u}}_i^n = \frac{\mathbf{F}_i^n}{m_i} \quad , \quad \dot{\mathbf{u}}_i^{n+1/2} = \dot{\mathbf{u}}_i^{n-1/2} + \ddot{\mathbf{u}}_i^n \Delta t \quad , \quad \mathbf{u}_i^{n+1} = \mathbf{u}_i^n + \dot{\mathbf{u}}_i^{n+1/2} \Delta t \tag{6}$$

221 A similar set of equations can be written for integrating in time the angular accelerations.

The explicit time integration scheme is chosen due to the high computational cost of the DEM solution for large problems. The stability of the scheme is conditioned to the time step value. The critical time step is related to the high frequency of the problem, (ω^{max}), i.e.

$$\Delta t \leq \Delta t_{cr} = \frac{2}{\omega^{max}} \left(\sqrt{1+\xi^2} - \xi \right) \tag{7}$$

222 where ξ is a fraction of the critical damping [4,30].

3.1.2 Forces acting over the discrete element

The interaction forces at the contact interface between two particles i and j ($\mathbf{F}^{ij}$) are obtained from the normal ($\mathbf{F}_n^{ij}$) and tangential ($\mathbf{F}_s^{ij}$) components (Figure 5b).

The normal component of the interaction forces is calculated as,

$$F_n^{ij} = \sigma_n \alpha_{ij} A^{ij} \quad \text{with } A^{ij} = \pi r_{c,ij}^2 \tag{8}$$

where σ_n is the normal stress at the contact interface, r_c is the minimum radius of the two interacting particles (Figure 5a) and α_{ij} is a parameter that dependes on the number of contacts and the packing of the particles [31]. In our work we have used a global definition of $\alpha_{ij} = \alpha = 40\frac{P}{N_c}$ where N_c and P are respectively the average number of contacts per sphere and the average porosity for the whole particle assembly [31]. The normal stress σ_n is calculated from the strain ξ_n and the strain rate $\dot{\xi}_n$ along the normal direction as,

$$\sigma_n = E\varepsilon_n + c\dot{\varepsilon}_n \tag{9}$$

where E is the Young modulus, c is a local damping parameter calculated as

$$c = 2\frac{\xi}{r_{c,ij}}\sqrt{m_{ij}K_n^{ij}} \quad \text{with} \quad m_{ij} = \frac{m_i m_j}{m_i + m_j} \tag{10}$$

where K_n^{ij} is the normal stiffness parameter (see Eq.(13)).

The normal strain and strain rate values are computed from the kinematic variables as,

$$\varepsilon_n = \frac{u_n}{d_{ij}} \qquad \dot{\varepsilon}_n = \frac{\dot{u}_n}{d_{ij}} \tag{11}$$

where u_n and $\dot{u}_n$ are the relative displacements and the relative velocity between two particles along the normal direction at the contact interface and d_{ij} is the distance between the centroids of the two particles (Figure 5b).

Equations (8)–(11) lead to a general relation between for the normal force and the kinematic variables as

$$F_n^{ij} = \frac{\alpha_{ij}A^{ij}}{d_{ij}}\left[Eu_n + 2\frac{\xi}{r_c}\sqrt{m_{ij}K_n}\dot{u}_n\right] = K_n^{ij}u_n + C_n^{ij}\dot{u}_n \tag{12}$$

where K_n^{ij} and C_n^{ij} are the normal stiffness and the normal viscous damping parameters at the contact interface between particles i and j that can be deduced from Eq.(12) as

$$K_n^{ij} = \frac{\alpha_{ij}A^{ij}}{d_{ij}}E \quad , \quad C_n^{ij} = \frac{2\alpha_{ij}A^{ij}\xi}{d_{ij}r_{c,ij}}\sqrt{m_{ij}K_n^{ij}} \tag{13}$$

A similar approach leads to the constitutive expression for the shear forces in the two tangential directions as [31]

$$\mathbf{F}_s^{ij} = K_s^{ij}\mathbf{u}_s^{ij} + C_s^{ij}\dot{\mathbf{u}}_s^{ij} \quad \text{with} \quad C_t^{ij} = \frac{2\alpha_{ij}A^{ij}\xi}{d_{ij}r_{c,ij}}\sqrt{m_{ij}K_s^{ij}} \tag{14}$$

where vector $\mathbf{u}_s^{ij}$ is the shear component of the relative displacements between particles, calculated as,

$$\mathbf{u}_s^{ij} = \mathbf{u}^{ij} - \left(\mathbf{u}^{ij}\mathbf{n}^{ij}\right)\mathbf{n}^{ij} \tag{15}$$

In Eq.(14) K_s^{ij} is the shear stiffness parameter at the contact interface (assumed to be the same for both shear directions), given by

$$K_s^{ij} = \frac{K_n^{ij}}{2\left(1+\nu\right)} \tag{16}$$

where ν is the Poisson's ratio of the material.

Additional damping forces can be computed from the application of a global damping over the set of particles. This damping component is characterized by translation (α^t) and rotation (α^r) damping parameters defined as a fraction of the stiffness parameters. In this work we have taken $\alpha^r = \alpha^t = 0,10$. The global damping forces act in opposite direction to the motion of the particles according to the following expressions:

$$\mathbf{F}_i^{damp} = -\alpha^t \left|\mathbf{F}_i^{ext} + \mathbf{F}^{ij}\right| \frac{\dot{\mathbf{u}}_i}{|\dot{\mathbf{u}}_i|} \tag{17a}$$

$$\mathbf{T}_i^{damp} = -\alpha^r \left|\mathbf{T}_i\right| \frac{\dot{\boldsymbol{\omega}}_i}{|\dot{\boldsymbol{\omega}}_i|} \tag{17b}$$

The local DEM constitutive model described above holds for cohesive (bonded) and non-cohesive materials. The latter is a particular case of the former, when the bonds between the particles are assumed to be initially broken. More details can be found in [31].

3.2 Normal and shear failure

Cohesive bonds at a contact interface are assumed to start breaking when the interface strength is exceeded in the normal direction by the tensile contact force, *or* in the tangential direction by the shear force. The *uncoupled* failure (decohesion) criterion for the normal and tangential directions at the contact interface between particles i and j is written as

$$F_{n_t} \geq \mathcal{F}_{n_t} \quad , \quad F_s \geq \mathcal{F}_s \tag{18}$$

where $\mathcal{F}_{n_t}$ and $\mathcal{F}_s$ are the interface strengths for pure tension and shear-compression conditions, respectively, F_{n_t} is the normal tensile force and F_s is the modulus of the shear force vector $\mathbf{F}_s^{ij}$ (Figure 5 and Eq.(14)).

The interface strengths are defined as

$$\mathcal{F}_{n_t} = \sigma_t^f \bar{A}^{ij} \quad , \quad \mathcal{F}_s = \tau^f \bar{A}^{ij} + \mu_1 |F_{n_c}| \tag{19}$$

where σ_t^f and τ^f are the tensile and shear strengths respectively, F_{n_c} is the compressive normal force at the contact interface and $\mu_1 = \tan\phi_1$ is a (static) friction parameter, where ϕ_1 is an internal friction angle. These values are assumed to be an intrinsic property of the material and are determined experimentally.

The tensile strength (σ_t^f) defines the maximum tensile stress that ice can resist before failure occurs. In [41], values of the tensile strength loaded across the columns of a sea ice sheet range between 0.2 MPa and 0.80 MPa. However, when loading take place with tensile stresses along the columns, that is in the direction of growth, the tensile strength is about three to four times higher, up to a maximum value of $\sigma_t^f = 2$ MPa. For the isotropic ice model used in this work we have chosen $\sigma_t^f = 1.6$ MPa.

As for the shear strength the value of $\tau^f = 1$ MPa has been used as recommended in [5] and [13].

Following tension failure, the constitutive behavior in the shear direction is governed by the standard Coulomb law

$$\mathbf{F}_s = \mu_2 |F_{n_c}| \frac{\mathbf{u}_s}{|\mathbf{u}_s|} \quad \text{with} \quad \mu_2 = \tan\phi_2 \tag{20}$$

where μ_2 is a dynamic Coulomb friction coefficient and ϕ_2 is the post-failure internal friction angle. Both parameters are determined from experimental tests.

Figure 6 shows the graphical representation of the failure criterium described by Eqs.(18), (19) and (20). This criterium assumes that the tension and shear forces contribute to the

failure of the contact interface in a decoupled manner. On the other hand, shear failure under normal compressive forces follows a failure line that is a function of the shear failure stress, the compression force and the internal friction angle.

Indeed, a coupled failure model in the tension-shear zone can also be used (Figure 6b) [31]. For the numerical tests presented in this work the uncoupled model has been used.

Figure 7 shows the evolution of the normal tension force F_{n_t} and the shear force modulus F_s at a contact interface until failure in terms of the relative normal and tangential displacement increments. Elastic damage under tensile and shear conditions can be taken into account by assuming a linear softening behaviour defined by the softening moduli H_n and H_t introduced into the force-displacement relationships in the normal (tensile) and shear directions, respectively (Figure 7). In this work H_n and H_t have been assumed to be a small percentage (5%) of the respective elastic module i, thus reproducing a quasi elasto-brittle behavior [31].

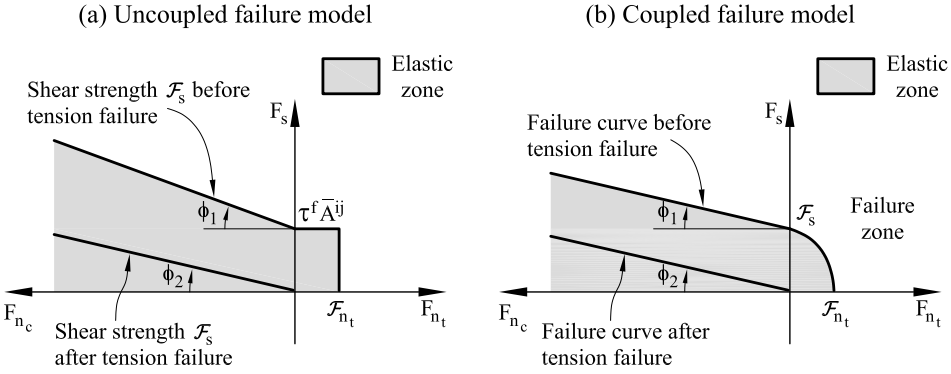

Figure 6: Failure line in terms of normal and shear forces. Uncoupled failure model. (b) Coupled failure model

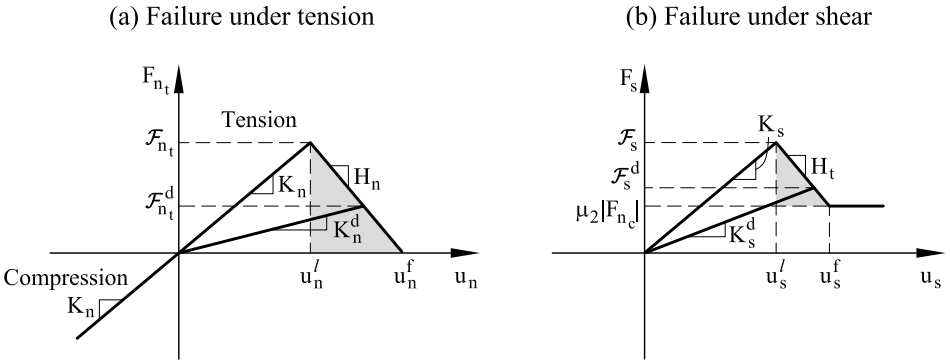

Figure 7: Undamaged and damaged elastic moduli under tension (a) and shear (b) forces

4 Sea ice computational parameters

4.1 Mechanical properties

The mechanical properties of sea ice required to carry out the numerical simulations with the elastic constitutive model described are obtained from values used in similar publications and reported laboratory and field measurements.

4.1.1 Young modulus

The value of the Young modulus of sea ice E is directly related with the temperature (T_i) and the brine volume (Φ_b) of sea ice, in such a way that it increases with decreasing temperature and decreasing brine volume. For very low brine volumes, E values are in the range of 9 to 10 GPa, resembling to that of freshwater ice. Increases in brine volume results in a weaker and softer sea ice and consequently, the Young modulus decreases. In [17] some tensile experiments were carried out on columnar sea ice at a strain rate equals 10^{-3} s^{-1}. The density of such ice was 910 kg/m^3 and a total porosity (sum of brine and air) of 2.3 out of 100. The reported values for the Young modulus was in the range of 6 GPa to 8.2 GPa, as it was considered a very low brine content. Usually the content of brine oscillates between 4.6 to 17 ppt and in these case the Young modulus is lower. For engineering applications it is common to use values of E between 1 to 9 GPa, depending on the physical characteristics of the sea ice used. In this work we will use values between 1 to 3 GPa, as reported in [5].

4.1.2 Poisson's ratio

Although some investigations have been done and several empirical equations have been proposed to estimate the Poisson's ratio of sea ice, further understanding of how to measure it is required [41]. For engineering applications $\nu = 0.33$ is mostly used and this is the value chosen in this work.

4.1.3 Ice-ice and ice-steel friction coefficients

Two friction coefficients are necessary in this work. On one hand, the ice-ice friction coefficient (μ_{ii}) for modeling contacts between isolated ice particles. A wide range of averaged values has been used for the ice-ice friction coefficient to carry out numerical simulations. Published values range between 0.03 and 0.08 [26]. A value of 0.05 has been used in this work for the ice-ice friction coefficient. On the other hand, the aim of this work is to study the interaction between ice and ships. For this purpose, the friction coefficient of ice-steel contact (μ_{is}) is of interest. In [41] some studies are reported about the friction behavior between ice and painted (smooth) steel. They concluded a value for the friction coefficient of 0.25, which is also used in our simulations.

5 Validation of the bonded-DEM in the analysis of the uniaxial compression strength of an ice specimen

The local bonded DEM presented in the previous section has been validated in the analysis of an uniaxial compression strength (UCS) for a cylindrical ice specimen of polycristal ice. The following material parameters have been assumed for the ice: Young modulus $E = 3$ GPa, Poisson's ratio $\nu = 0.33$, ice-ice friction coefficient $\mu = 0.05$, tensile failure strength $\sigma_t^f = 2$ MPa. Figure 8 shows the axial strength-axial strain curve. The failure stress value is 22.9 MPa which agrees well with the expected value for polycristal ice. Figure 9 shows the ice specimen at different instants of the loading process.

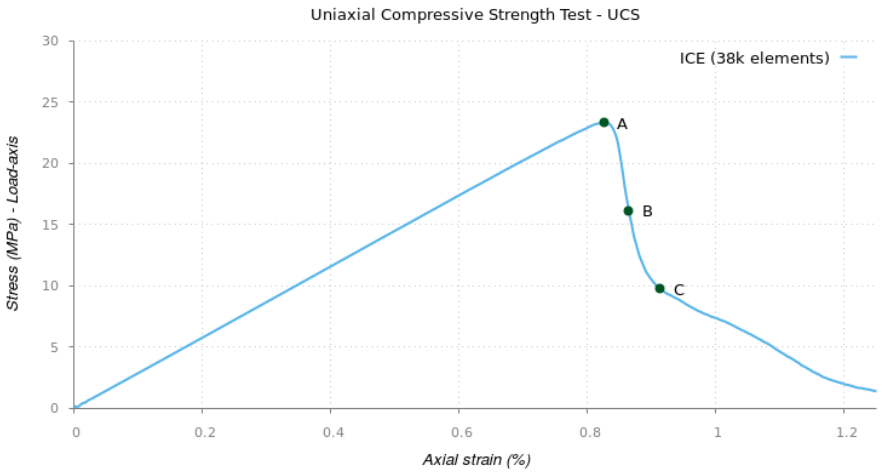

Figure 8: DEM analysis of UCS experiment on polycristal ice using 38000 spherical elements.

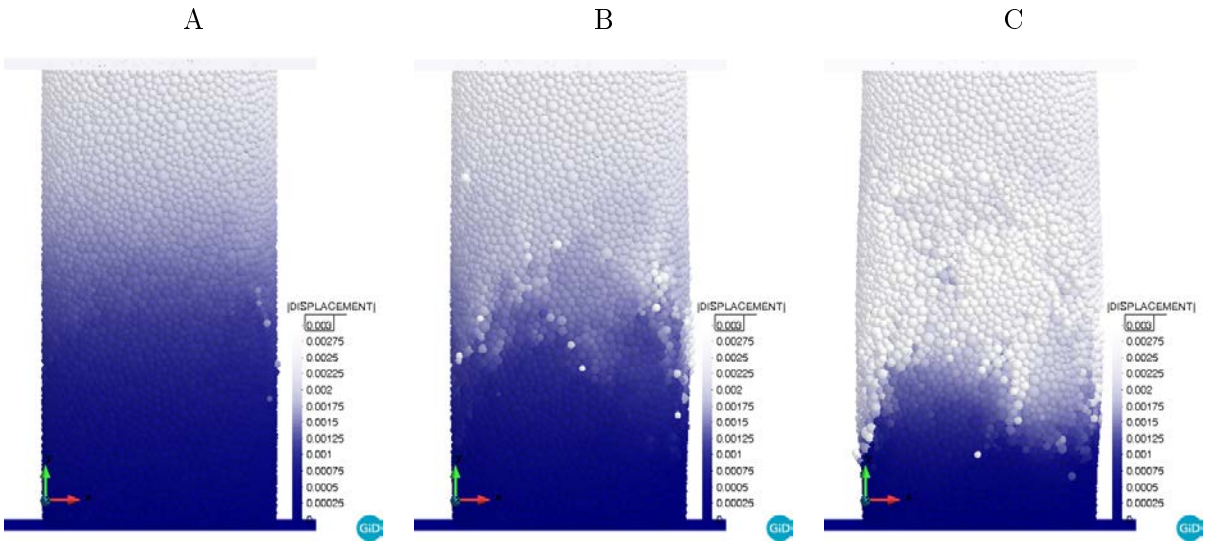

Figure 9: UCS experiment on polycristial ice analyzed with the bonded DEM. Views of the ice specimen at different instants of the loading process (points A, B and C of Figure 8).

6 Sloping structures-ice DEM simulations

This section presents the numerical simulations of the interaction of sloping structure and ice blocks carried out with the bonded DEM presented in the previous sections. They are split in three groups: ice loads computation on ice-breaking cones, ice cakes and floe-ice fractures and ship-ice interactions in unbroken level ice fields. In this paper we only include some examples. More applications can be found in [15].

The ice sheet is modeled as an arrangement of discrete elements randomly placed and bonded between each other at the contact points. The cohesive bonds can be broken, allowing to simulate the fracture of the material by setting the limitations on the tensile and shear strengths, as explained earlier.

6.1 Ice loads computation on ice-breaking cones

In the Bohai Sea of China there are several jacket platforms to perform different exploitation works such as research activities and oil & gas extraction. In the legs of the platforms it is common to install ice-breaking cones. These are conical elements which can break the incoming level ice in a flexural dominant mode.

In this work, a single leg of the jacket platforms JZ20-2 MNW and MUQ has been digitally modeled and loaded by an advancing level ice sheet. In most cases the cones include a top upper part and a bottom lower part. In this way the double cone height can cover the tidal height in the site.

Three different simulations have been performed varying the slope angle in which the ice sheet breaks. The influence of such slope into the magnitude of the generated ice loads is studied. In the first case studied the upper cone angle is 60^o whereas the lower one is 45^o. In a second set of simulations the geometry is modified changing the slope of the upper cone to 45^o. In Table 2 the geometrical parameters of the modeled system are listed.

Definitions	**Symbols**	**Values**	**Units**
Ice cover size	LxB	10x15	m^2
Ice thickness	h_i	0.2	m
Freeboard	w_f	0.02	m
Upper conical angle	θ_1	45 & 60	^{o}
Lower conical angle	θ_2	45	^{o}
Cone height	h_{cone}	4	m

Table 2: Geometrical parameters of the conical structure and the ice sheet.

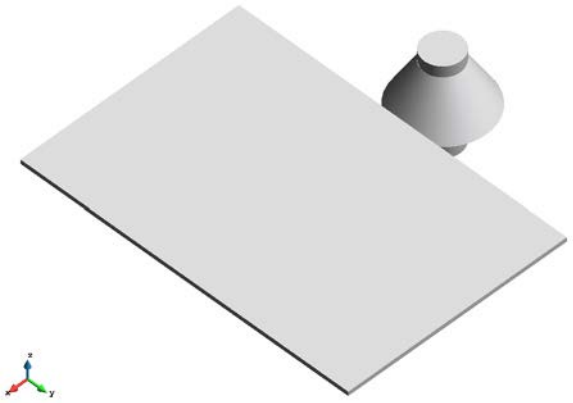

Figure 10: Isometric view of the modeled cone system and the ice sheet.

Table 3 lists the computational parameters for the ice material. The boundary conditions set to the ice sheet are simply to impose motion. Therefore, the particles at the far end and side boundaries move at a constant velocity in the ice advancing direction (the -X direction the drawings). In order to simulate an infinite domain, the side motion of the ice sheet is constrainted.

Definitions	Symbols	Values	Units
Type of ice	-	Level ice	-
Ice velocity	v_i	0.5	m/s
Density of sea ice	ρ_i	920	kg/m^3
Young Modulus of sea ice	E	1e+9	Pa
Poisson ratio of sea ice	ν	0.33	-
Friction angle of sea ice	ϕ_i	30	^{o}
Ice-ice (static) friction	μ_{ii}	0.05	-
Ice-structure (static) friction	μ_{is}	0.25	-
Normal tensile strength	σ_t^f	1.6	MPa
Shear strength	τ^f	1	MPa

Table 3: Computational parameters for the ice material.

Table 4 lists the computational parameters for the conical structure.

Definitions	Symbols	Values	Units
Type of structure	-	Conical	-
Motion	-	Fixed	-
Young Modulus	E_s	200e+8	Pa
Poisson ratio	ν_s	0.265	-

Table 4: Computational parameters for the conical structure.

Finally, parameters for the DEM simulation are listed in Table 5.

Definitions	Symbols	Values	Units
Mesh packing	-	Unstructured	-
DE type	-	Spheres	-
DE diameter	d_s	0.07 (3 layers)	m
# of DE	N_p	93257	-
Time step	Δt	1.0e-5	s
Simulation time	T_t	22	s
Calculation time	-	3.25 & 4.11	days
# CPUs	-	20 & 16	CPUs

Table 5: DEM analysis parameters.

For space limitation reasons only the results of the cone breaking against the 60^o upper cone are discussed. Results for the other cases are shown in the comparison graphs and tables.

6.1.1 Level ice breaking against a 60^o upper cone

Figure 11 shows the evolution of the simulation at different time steps. The ice sheet drags the whole domain, creating a channel behind the cone. At the first contacts ice breaks mostly in a crushing mode and some particles are thrown out with relatively high velocity. While the ice sheet keeps advancing, in the vicinity of the contact zone ice breaks mostly by bending. Ice blocks of different sizes are generated and rubbled up on the ice sheet and behind the cone.

During the calculation the evolution of the interaction force has been computed at the ice-cone contact zone.

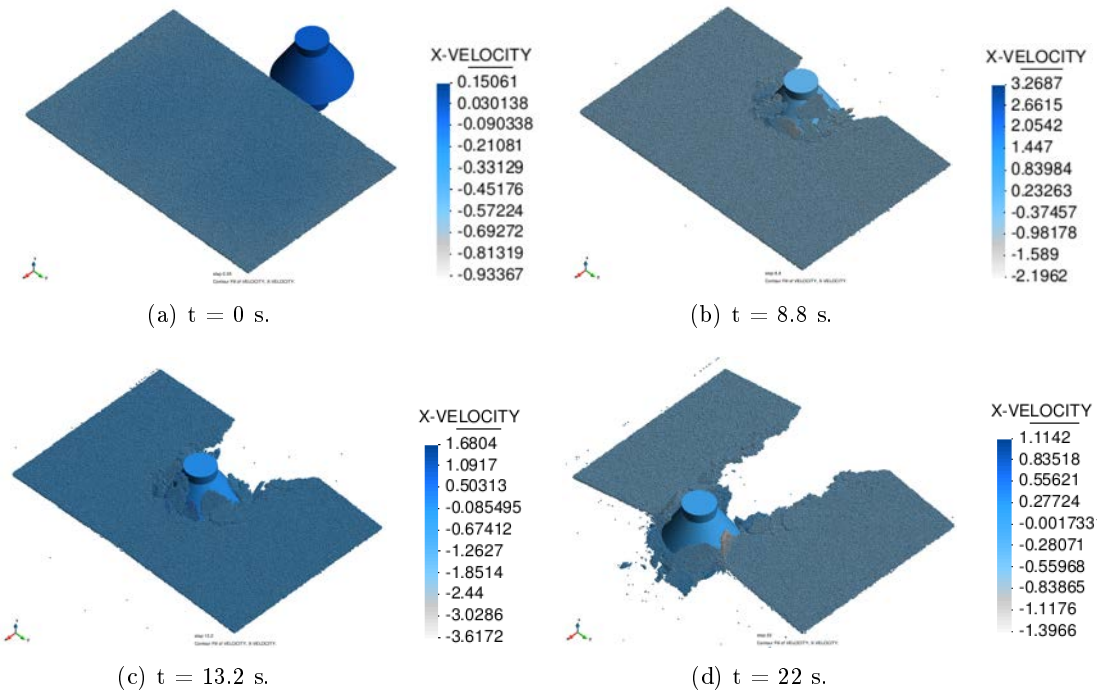

(a) t = 0 s. (b) t = 8.8 s.

(c) t = 13.2 s. (d) t = 22 s.

Figure 11: Interaction between ice cover and upper cone (60^o) simulated with the DEM. The magnitude of the X-velocity of each particle is presented in different colors. The color of the structure is always refered to 0 m/s.

Figures 12 and 13 show, respectively, the evolution of the X and Z-components of the ice force. The peaks are not representative and, therefore, the data has been smoothed by taking the median over a window of 100 data points. For the X-component the smoothed values fluctuate between 88.7 kN to 8.1 kN (minimum), while for the Z-component (vertical) they oscillate between 36.9 kN (maximum) to 3.8 kN (minimum).

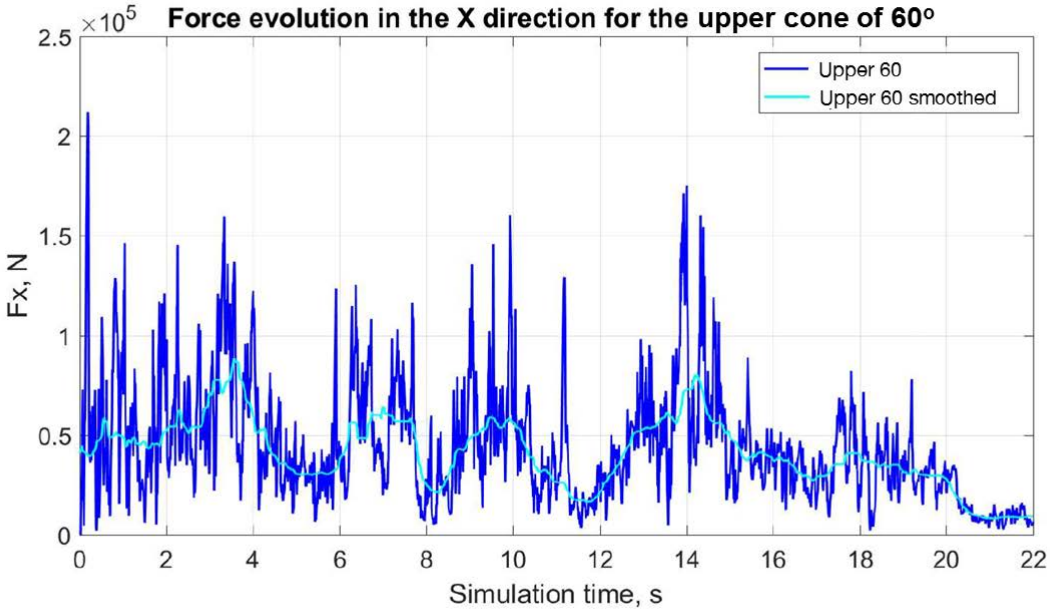

Figure 12: Force evolution in the X direction for the 60^o upper cone.

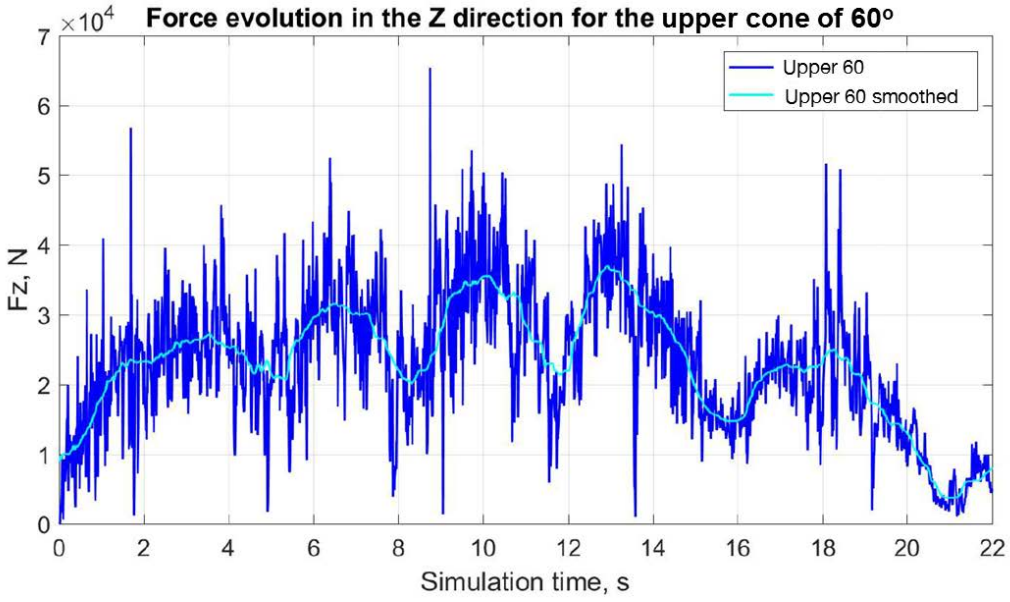

Figure 13: Force evolution in the Z direction for the 60^o upper cone.

6.1.2 Level-ice breaking against a 45^o upper cone

The last numerical simulation presented is the one of a modified upper cone. The upper cone angle has been changed to 45^o in order to see the influence of lower slopes on ice loads.

In principle, the failure mode and the ice sheet behaviour is expected to be similar to the 60^o upper cone case. In Figure 14 several snapshots are presented to follow the evolution of the ice sheet which drags the computational domain with a constant velocity and breaks against the conical structure.

Firstly, one realises that the crushing effect produced at the first contacts in the 60^o upper cone vanish for the 45^o one. This is a positive result as the crushing failure mode is expected to appear in vertical structures. Hence, crushing is alleviated by decreasing the upper slope angle from 60^o to 45^o.

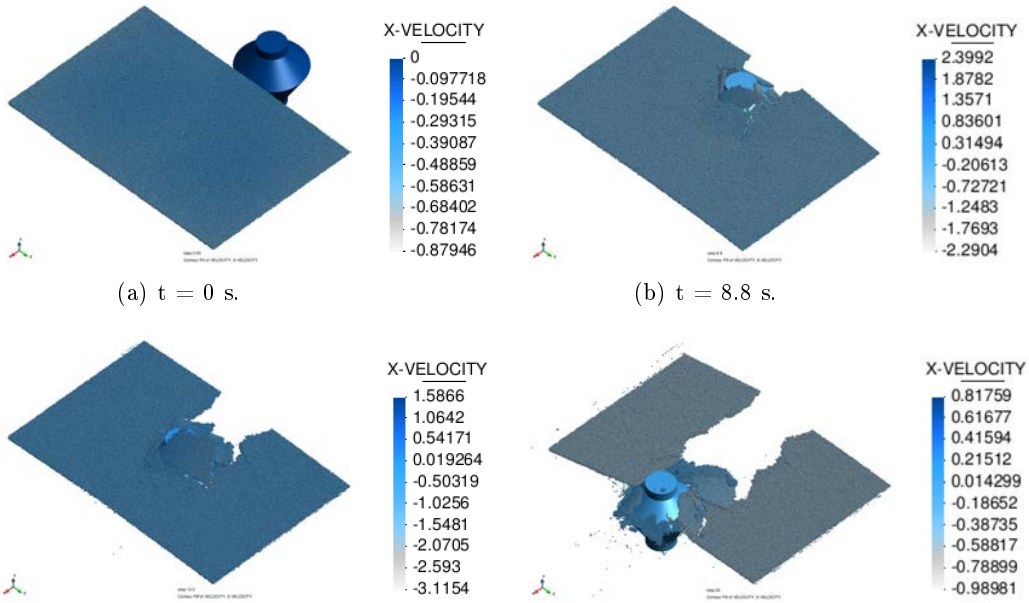

(a) t = 0 s. (b) t = 8.8 s.

(c) t = 13.2 s. (d) t = 22 s.

Figure 14: Interaction between ice cover and upper cone (45^o) simulated with DEM. The magnitude of the X-velocity of each particle is presented in different colors. The color of the structure is refereed to 0 m/s.

Figure 15 shows the evolution of the X component of the ice force. The peaks in there are not representative and, therefore, the data has been smoothed by taking the median over a window of 100 data points.

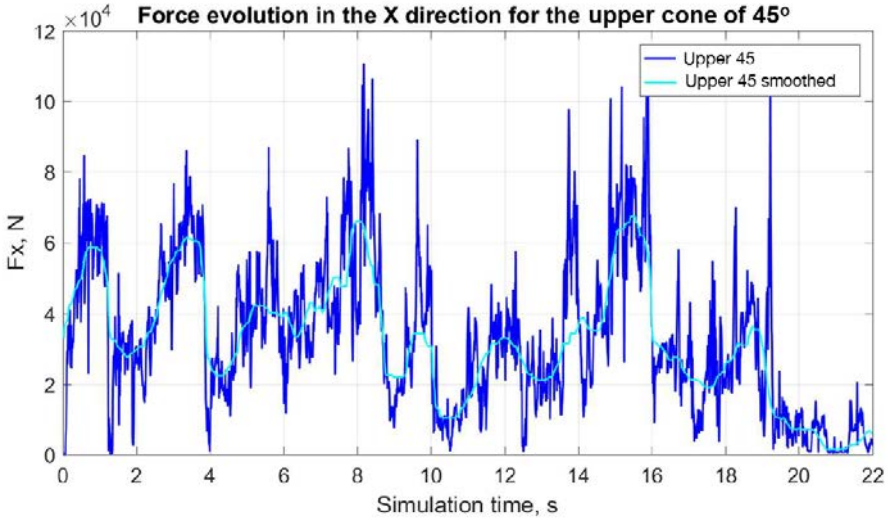

Figure 15: Force evolution in the X direction for the 45^o upper cone.

The smoothed force values fluctuate between 67.3 kN (maximum) to 1.5 kN (minimum).

Figure 16 shows the evolution of the Z component of the ice force. The computed values have been smoothed in order to obtain representative results.

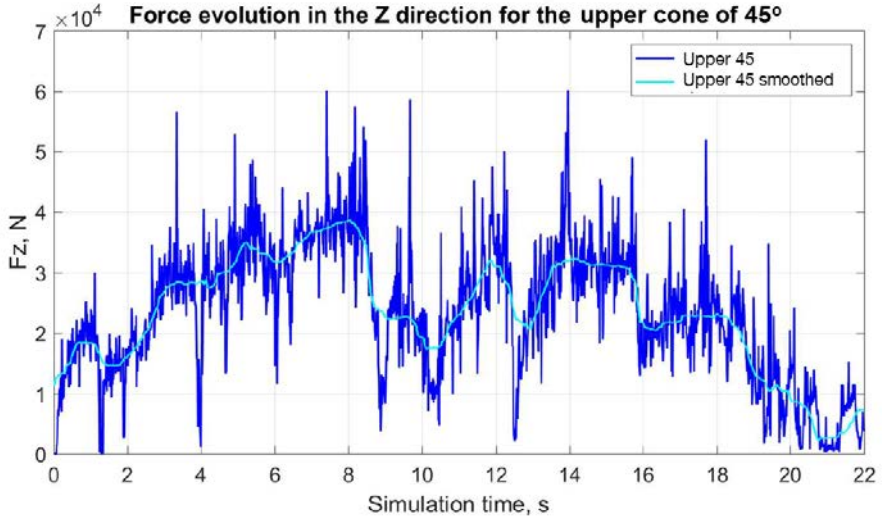

Figure 16: Force evolution in the Z direction for the 45^o upper cone.

The smoothed force values fluctuate between 38.6 kN (maximum) to 2.2 kN (minimum).

6.1.3 Level-ice breaking against a 45^o lower cone

If the tidal lowers occasionally the incoming ice sheet will break against the lower part of the double cone configuration.

Because the slope of the lower part of the cone is smallen than the upper one, the forces are also expected to be smaller.

Figure 17 shows the evolution of the ice sheet breaking against the lower part of the 45^o lower cone. The snapshots show how the ice sheet bends lower. Firstly a radial crack is generated, followed by subsequent semi-radial cracks to the sides which induce the failure of the ice sheet into big pieces.

At the last steps of the simulation the sides of the ice cover are broken, and thus the boundary conditions and the assumption of infinite domain does not longer hold. This highlights the need for a larger width of the modelled domain.

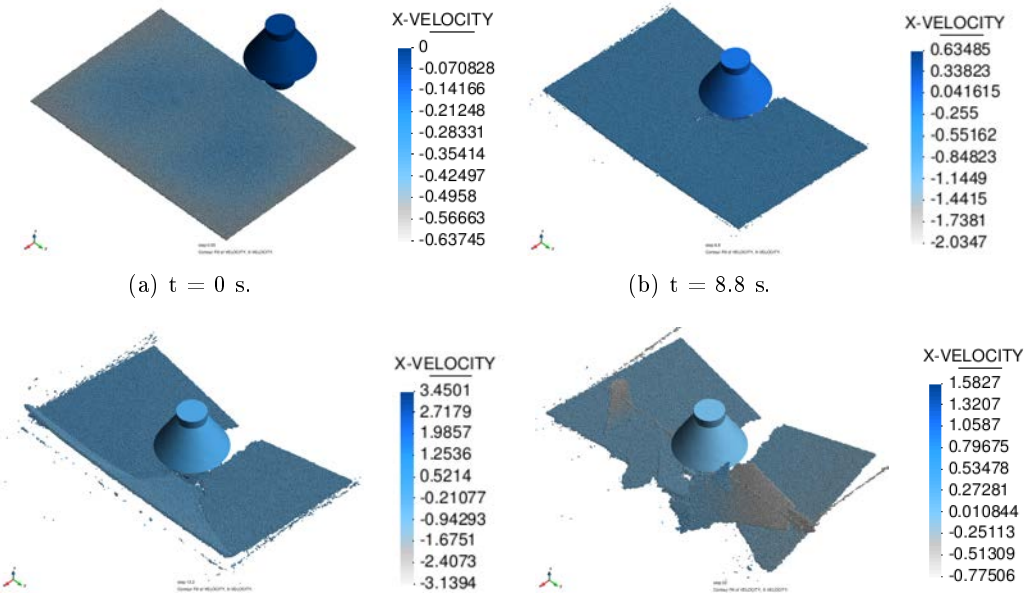

(a) t = 0 s. (b) t = 8.8 s.

(c) t = 13.2 s. (d) t = 22 s.

Figure 17: Interaction between ice cover and lower cone (45^o) simulated with DEM. The magnitude of the X-velocity of each particle is presented in different colors. The color of the structure is refereed to 0 m/s.

Figure 18 shows the evolution of the X component of the ice force. The peaks are not representative and, therefore, the data has been smoothed by taking the median over a window of 100 data points.

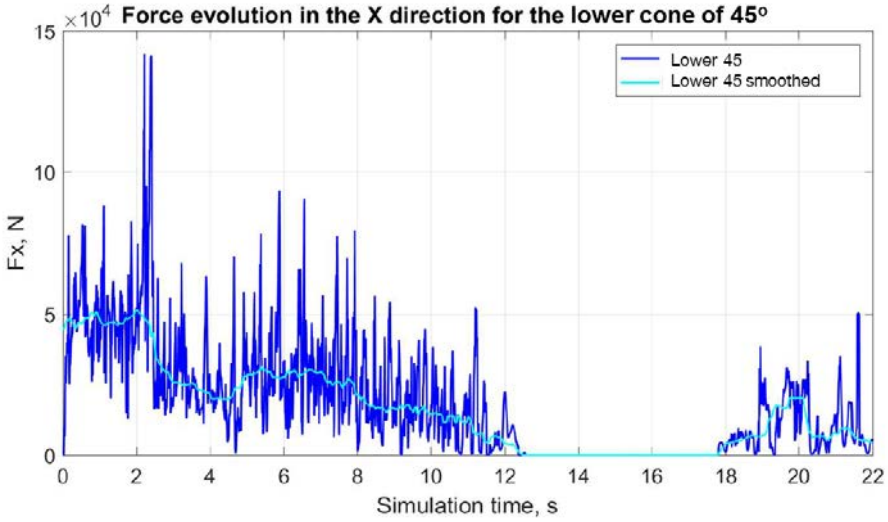

Figure 18: Force evolution in the X direction for the 45^o lower cone.

The smoothed values fluctuate between 51.1 kN (maximum) to 0 kN (minimum). Zero forces are produced between the simulated seconds 13 and 17.5. This gap is due to the non existence of ice-structure contacts.

Figure 19 shows the evolution of the Z component of the ice force. One more the computed values have been smoothed in order to obtain representative results.

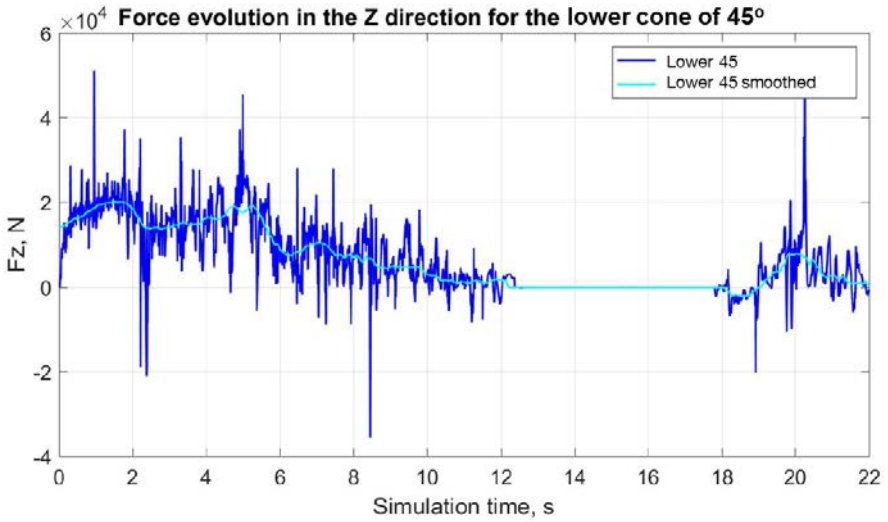

Figure 19: Force evolution in the Z direction for the 45^o lower cone.

The smoothed values fluctuate between 20.1 kN (maximum) to 0 kN (minimum). The reason of zero forces is the same as commented few lines above.

6.1.4 Influence of cone slope

Both slopes (45^o and 60^o) when breaking against the upper part show similar behavior. However, when breaking against the lower part, the ice loads decrease in magnitude. Also, comparing the breaking patterns one realizes that the crushing effect produced at the first contacts in the 60^o upper cone vanishes for the 45^o one. This is a positive result because the crushing failure mode is expected to appear in vertical structures. So, crushing is alleviated by decreasing the cone slope from 60^o to 45^o. These results have an engineering interest.

Figure 20 shows the maximum horizontal and vertical components of the ice loads under the tested cone slopes.

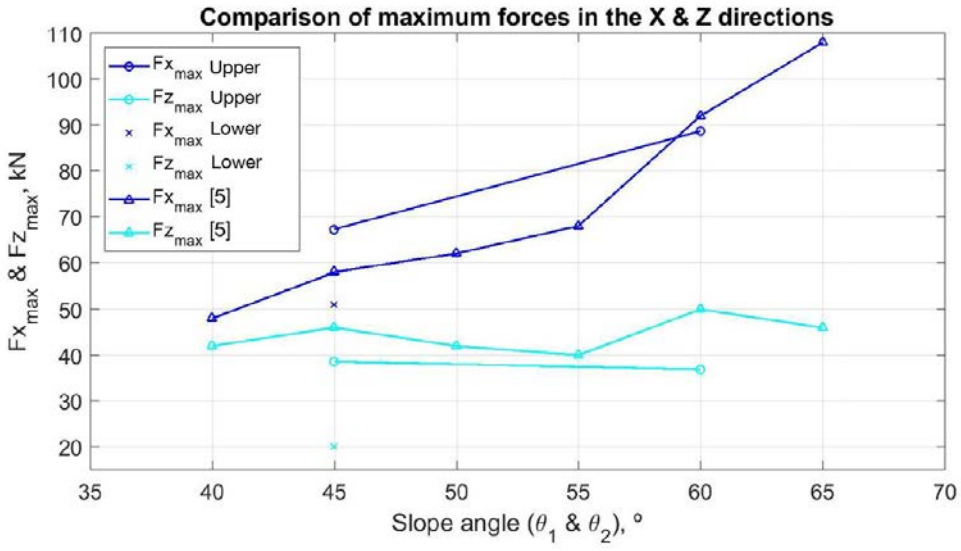

Figure 20: Maximum ice forces in the X and Z directions for different cone slope angles.

Cone configuration	$\mathbf{F}_{x_{max}}$		$\mathbf{F}_{z_{max}}$	
Upper 60^o	88.7	kN	36.9	kN
Lower 45^o	51.1	kN	20.1	kN
Upper 45^o	67.3	kN	38.6	kN

Table 6: Maximum ice loads in the X and Z directions for the three cone simulations.

For the maximum force values, the behavior indicates that the magnitude of the ice load in the X direction increases with increasing cone slope. Conversely, the magnitude of the ice load in the Z direction has not an obvious effect with the change of cone slope, because the values keep almost constant.

Additionally, for the maximum ice loads the effect of breaking against the lower part of the cone instead of the upper one produces a clear reduction in the force magnitude.

Our DEM results agree with DEM results reported in [5] in which similar simulations where performed, but with more slope angles and slightly different parameters.

The blue lines (both dark and light) with triangle dots in Figure 20 are the results of [5] and the blue lines (both dark and light) with circle dots are the ones obtained in this work. The trend of both sets of results is the same, with some little differences in the values.

6.2 Ice cakes and floe-ice fractures

During Arctic navigation, ships can encounter broken ice fields composed of separated ice floes with different dimensions, shapes and concentrations. In this section we study the interaction between an ice-breaking ship and separate ice floes, which has different dimensions, thickness and shapes. The simulated system consists of a digital model of a theoretical ship bow advancing with a constant speed in one direction towards the modeled ice floe. Thus, the numerical simulation is of a Single Degree of Freedom (SDF) motion.

This simulations are described by two elements: the ship bow and the modeled ice floe. The ship bow is considered as a solid with imposed motion and discretized with finite elements, whereas the ice floe is composed by an arrangement of bonded spherical particles. For the ship bow, a generic model has been created reproducing the main characteristics of a real ice-breaking ship. A stem buttock angle equals to 30^o and a draft of 7 meters has been considered. Figure 10 shows different views of the ship bow chosen.

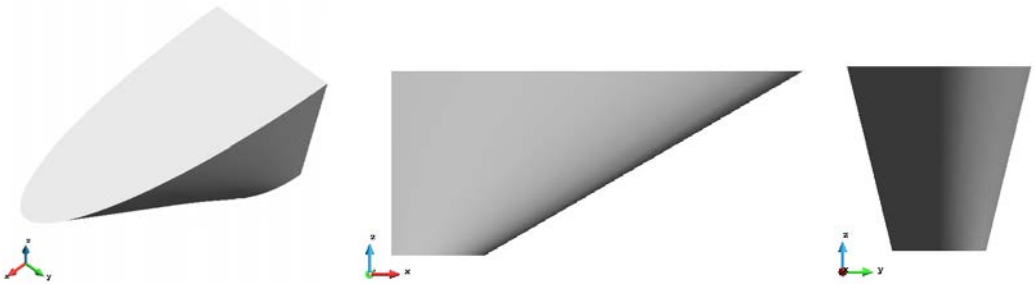

(a) Isometric view. (b) Side view. (c) Front view.

Figure 10: CAD views of the digital ship bow model.

In Table 7 the computational parameters for the ice material are listed. There are not boundary conditions set to the ice sheets because the aim is to simulate a separate ice floe without contacts with neighboring floes.

Definitions	**Symbols**	**Values**	**Units**
Initial ice velocity	v_i	0	m/s
Density of sea ice	ρ_i	920	kg/m^3
Young modulus of sea ice	E	3e+9	Pa
Poisson ratio of sea ice	ν	0.33	-
Friction angle of sea ice	ϕ_i	30	^{o}
Ice-ice (static) friction	μ_{ii}	0.05	-
Ice-structure (static) friction	μ_{is}	0.25	-
Normal tensile strength	σ_t^f	1.5	MPa
Shear strength	τ^f	1.0	MPa

Table 7: Computational parameters for the ice material.

Table 8 lists the computational parameters for the ship bow.

Definitions	Symbols	Values	Units
Type of structure	-	Ship bow	-
Structure velocity	v_s	2.06 (4)	m/s (kn)
Young modulus	E_s	200e+9	Pa
Poisson ratio	ν_s	0.265	-

Table 8: Computational parameters for the ship bow structure.

Table 9 lists some of the numerical computational parameters. Other parameter will be listed in each group of the following simulations.

Definitions	Symbols	Values	Units
Mesh packing	-	Unstructured	-
DE type	-	Spheres	-

Table 9: DEM analysis parameters.

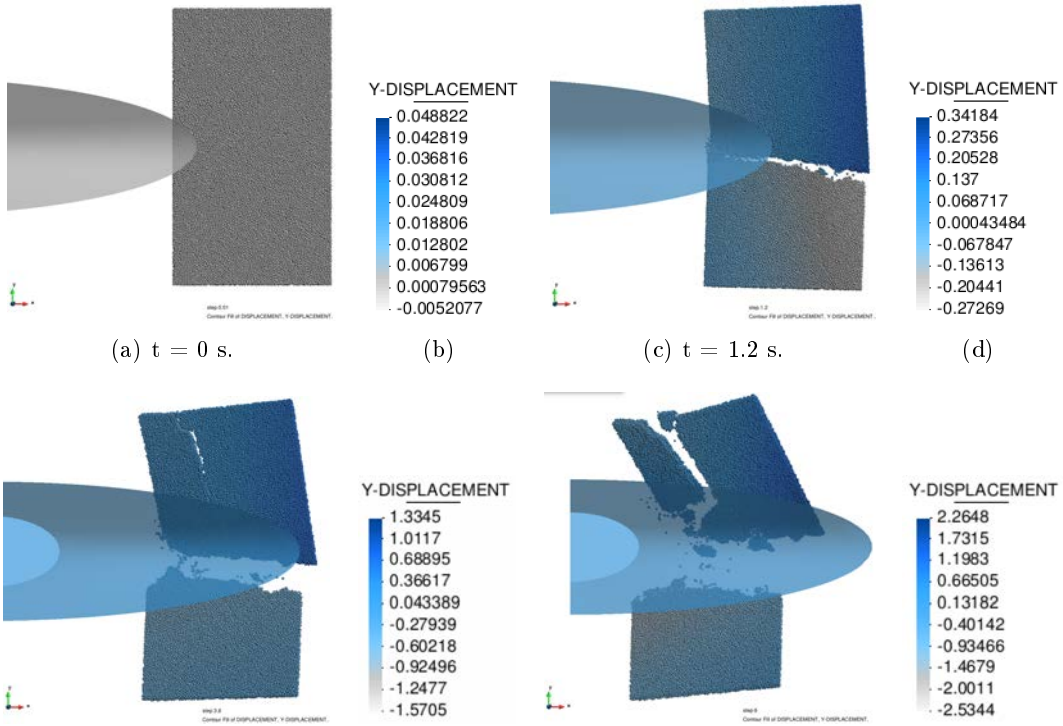

(a) t = 0 s. (b) (c) t = 1.2 s. (d)

(e) t = 3.6 s. (f) (g) t = 6 s. (h)

Figure 22: Interaction between the ship bow and finite size wide ice floe simulated with the DEM. The magnitude of the Y-displacement is presented in different colors.

A total of twenty simulations have been carried out, five for each of the four ice thickness (h_i). The considered thickness are 0.5, 1.0, 1.5 and 2.0 meters because the first-year sea ice thickness ranges from 0.3 to 2.0 meters. For extension reasons, we only discuss the results of the numerical simulation of an ice thickness of 0.5 m considering a finite size wide ice floe.

In this group of simulations the floe dimensions must fulfill the condition $l \leq \mathrm{L} \leq 2l$. The selected sizes are shown in Table 10. The DEM analysis parameters are those of Table 9.

Definitions	**Symbols**	**Values**	**Units**
Floe shape	LxB	wide	-
Ice thickness	h_i	0.5	m
Floe size	LxB	8x14	m^2
DE diameter	d_s	0.125	m
# of DE	N_p	30554	-
Time step	Δt	1.0e-5	s
Total simulation time	T_t	6	s
Calculation time time	-	7.03	hours
# CPUs	-	20	CPUs

Table 10: Geometrical and DEM analysis parameters for the wide ice floe of 0.5 m thick.

Figure 22 shows the evolution at different time steps of the simulation with interaction between the ship bow and an ice floe of 0.5 m thickness and 8x14 m^2.

Observations on the simulation results highlight how the wide ice floe is first submerged a bit. This produces that the lower part of the ice floe is under tension while the upper part is in compression. Consequently, a radial crack is initiated from the contact zone and propagated to the end boundary. Approximately at the simulation time of 2.5 s, the wide ice floe is fully broken in two parts. Both points can move freely but subjected to buoyancy. Thus, they progressively try to recover the equilibrium state but the ship bow maintains its advancing motion and thus more contacts are produced between the separate parts and the ship hull. The created lead by the ship allows it to advance without difficulties. Looking at Figure 22 one can see how the Y-displacement increases from 0 m to around 2.25 m.

Figures 23, 24 and 25 show, respectively, the evolution of the X-, Y- and Z-components of the ice load. Again, the load peaks are not representative and therefore, the data has been smoothed by taking the median over a window of 100 data points.The smoothed values fluctuate between 196.9 kN (maximum) to 0 kN (minimum) for the X direction, between 74.2 kN (maximum) to -59.0 kN (minimum) for the Y direction and between 120.7 kN (maximum) to 0 kN (minimum). Figure 26 shows the maximum horizontal and vertical components of the ice loads versus the tested ice thicknesses.

Ice thickness (h_i)	$\mathbf{F}_{x_{max}}$		$\mathbf{F}_{y_{max}}$		$\mathbf{F}_{z_{max}}$	
0.5 m	196.9	kN	74.2	kN	120.7	kN

Table 11: Maximum ice loads in the X, Y and Z directions for the wide ice floe of 0.5 m thickness.

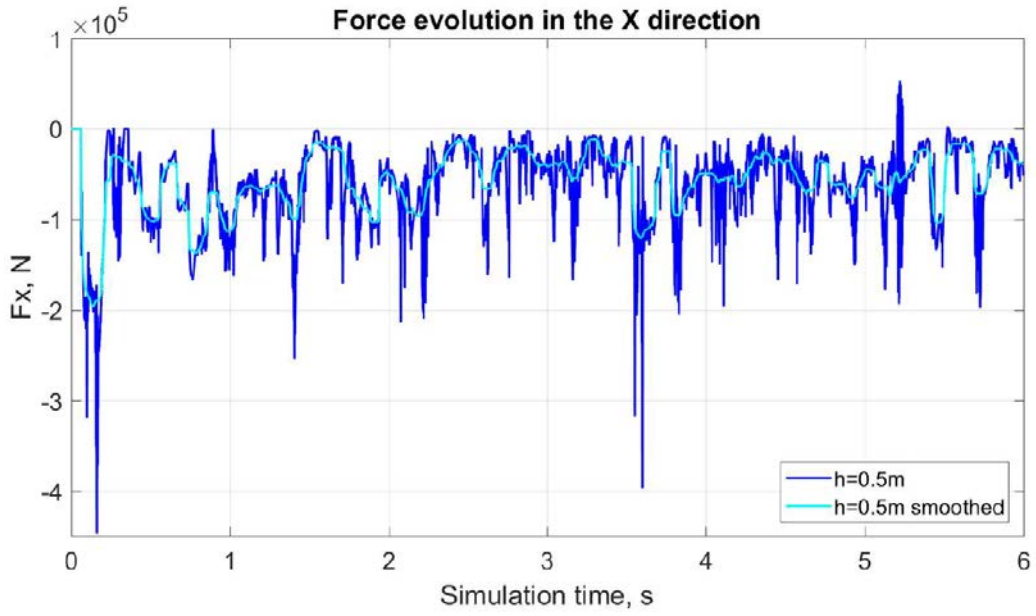

Figure 23: Evolution of the force in the X direction for the ice floe of 0.5 m thickness.

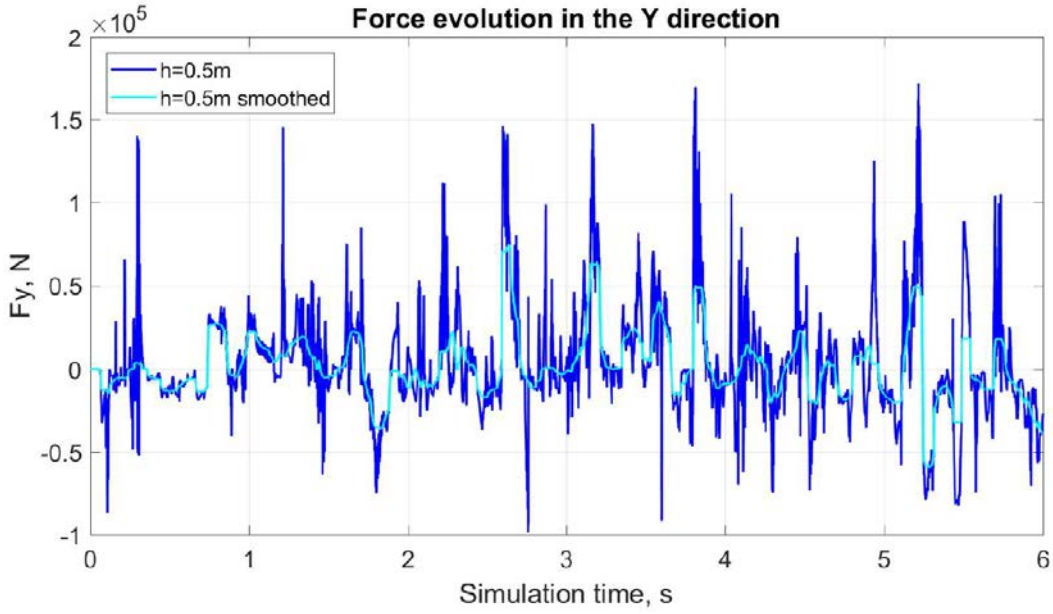

Figure 24: Evolution of the force in the Y direction for the ice floe of 0.5 m thickness.

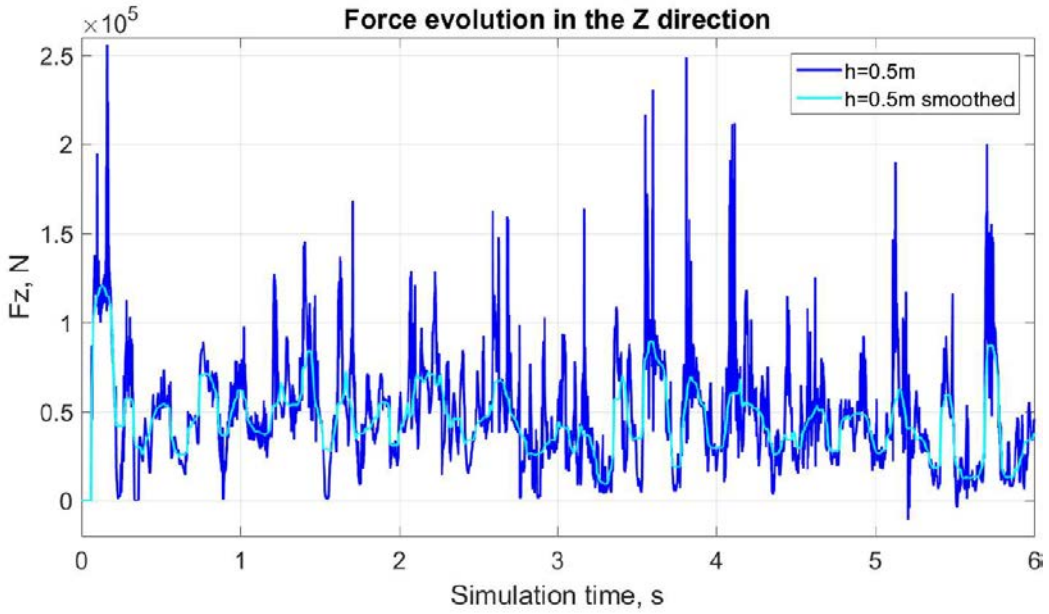

Figure 25: Evolution of the force in the Z direction for the ice floe of 0.5 m thickness.

Figure 26 shows our DEM results of the ice loads obtained for ice floes of different thicknesses (0.5, 1, 1.5 and 2 mts). The dark blue line with circle dots are the results for the X-component of the force, the black line with circle dots are the results for the Y-component, and the light blue line corresponds to the Z-component. The trend in the three components is the same, with some little differences in the values. For the maximum values, the behavior shows that the magnitude of the ice load in the X direction increases considerably with the ice thickness. Conversely, the magnitude of the ice loads in the Y and Z directions are smaller than for the X-component, but still increase with the ice thickness.

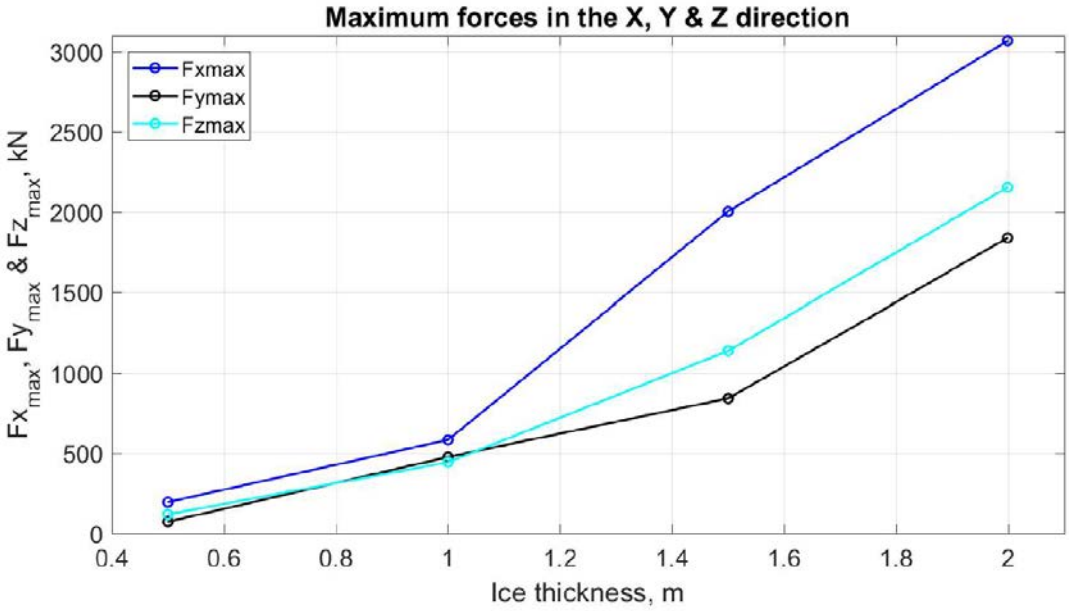

Figure 26: Comparison of maximum forces in the X, Y and Z directions for different ice floe thicknesses.

Because fracture occurs it is interesting to analyse the required propulsion power. This can

be computed as

$$P = F \cdot v \tag{21}$$

where F and v are the maximum ice load and the ship speed, respectively.

Referring to the maximum of the axial ice loads, which is 3068.7 kN (case of $h_i = 2$ m), the associated propulsion power is therefore $P = 6321.5$ kW (notice that the ship speed is v = 2.06 m/s).

6.2.1 Influence of ice thickness and floe dimensions

In this section we present a compilation of the maximum forces obtained for each numerical simulation in order to understand the effects that the ice thickness and the floe dimensions have on these forces. It is expected that when the ice thickness and the dimensions of the ice floe increase, the magnitude of the ice loads also increases, as the heavier and bigger the ice floe is, more power is needed to break it. The types of floe follow the terminology used in Section 2.2.

Figure 27 shows a summary of the ice loads in the X direction. For each ice thickness, the associated maximum force is plotted. The trend shows that when ice thickness increases, the ice load increases as well. The maximum ice loads in the X direction increase from 100 kN ($h_i = 0.5$ m) up to 4300 kN ($h_i = 2.0$ m).

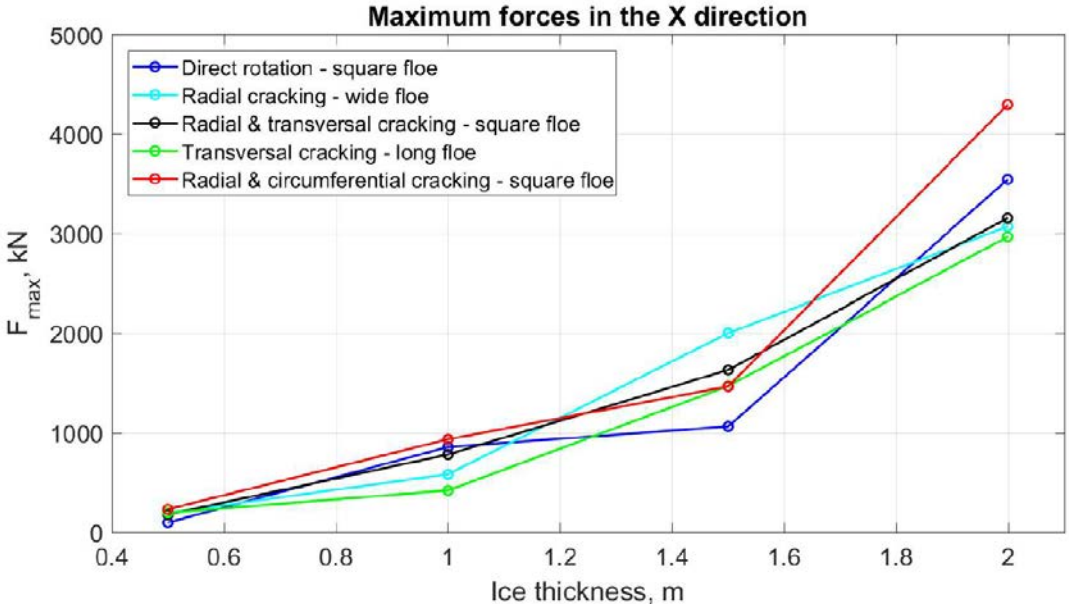

Figure 27: Ice loads in the X direction for different ice floe thicknesses.

Figure 28 shows results for the ice loads in the Y direction. Similarly as for the X-component, when ice thickness and dimensions increase, the ice load also increases. The maximum ice loads in the Y direction increase from 17 kN ($h_i = 0.5$ m) up to 2225 kN ($h_i = 2.0$ m).

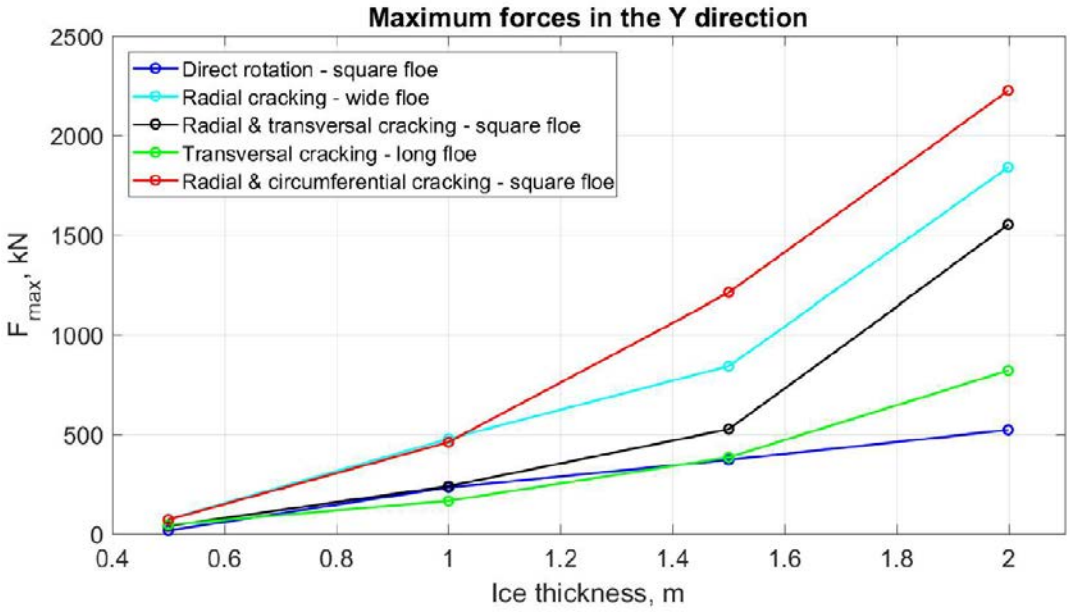

Figure 28: Ice loads in the Y direction for different ice floe thicknesses.

Finally, Figure 29 shows the ice loads in the Z direction. Here it can be seen the same behaviour as for the X and Y-components, that is, when ice thickness and dimensions increase, the ice load does the same. The maximum ice loads in the Z direction range from 69 kN ($h_i = 0.5$ m) up to 2350 kN ($h_i = 2.0$ m).

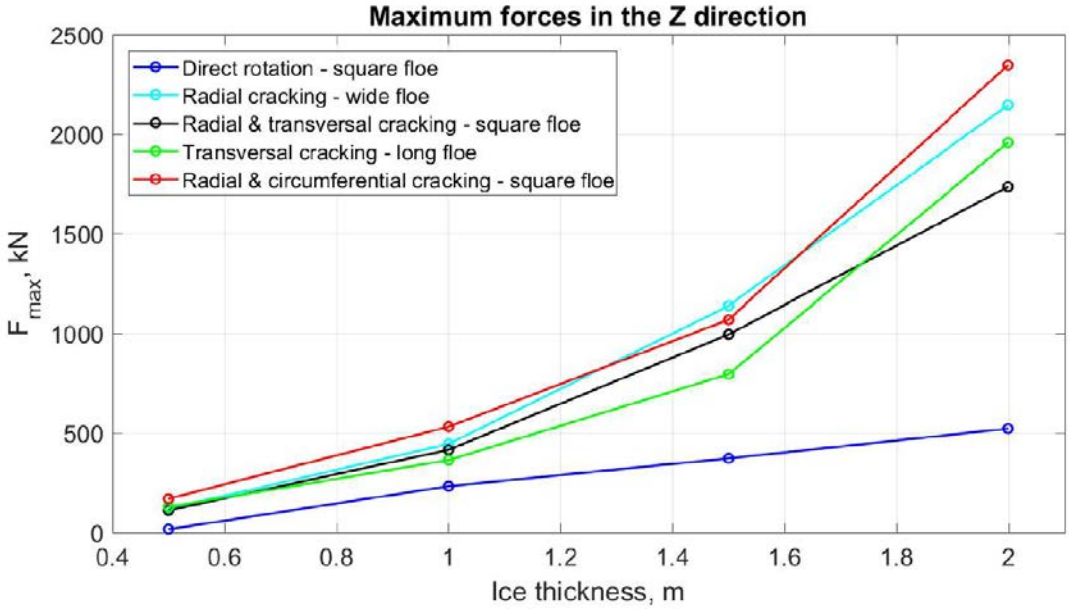

Figure 29: Ice loads in the Z direction for different ice floe thicknesses.

Summarizing, the ice thickness has a direct and proportional effect on the value of the ice loads. In general, the direct floe rotation simulations are the ones with smaller ice loads, as the dimensions are the smaller too. Also, the semi-infinite size floe simulations are the ones with larger ice loads. The other groups of ice floes have pretty similar behavior, except for the Y-component.

6.3 Ship-ice interactions in unbroken level ice fields

This section presents results for a ship navigating through a frozen sea formed by a continuous ice platform, represents a level ice sheet. When an ice-breaking vessel advances through a continuous and vast level ice sheet, two failure modes are likely to appear around the ship and in its local vicinity: the local crushing (mostly at the beginning contacts) and the local out-of-plane flexural mode. Sometimes another failure mode called global in-plane splitting it has been observed in the field. It produces long cracks that travel along the ice floe and open a lead. The conditions for these cracks to appear are specific, and when confinement is present they are difficult to be generated.

The simulated system consists of a 3D digital model created for a real ice-breaking ship. Specifically, the Tor Viking II has been used and it is forced to advance with a constant speed (its maximum capacity) in one direction towards the modeled level ice sheet. Thus, the numerical simulation is of a Single Degree of Freedom (SDF) motion.

This ship is classified with the class: DNV 1A1 ICE-10 Icebreaker (for max draft of 6.8m) Tug/Supply vessel, what means that can navigate in winter ice with pressure ridges and nominal ice thickness of 1.0 m. Its main dimensions are listed in Table 12.

Definitions	**Symbols**	**Values**	**Units**
Length o. a.	L_{oa}	83.7	m
Length between perp.	L_{pp}	75.2	m
Beam	B_s	18.0	m
Draft	T_s	6.8	m
Buttock angle at the stem	γ	24	^{o}

Table 12: Main dimensions of the Tor Viking II ice-breaking vessel.

In Figure 30 three views of the ice-breaking ship model are presented.

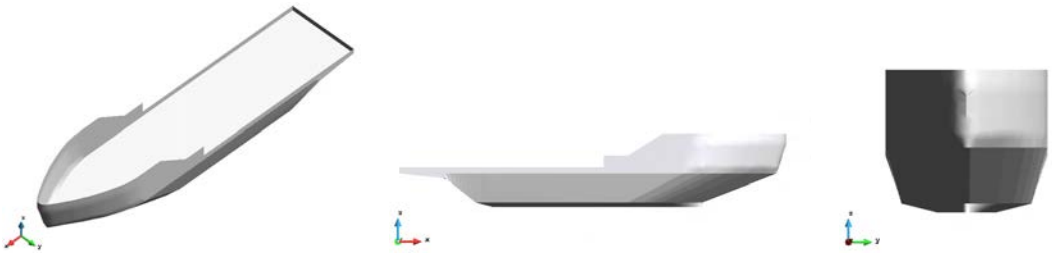

(a) Isometric view. (b) Side view. (c) Front view.

Figure 30: CAD views of the digital Tor Viking II ice-breaking ship model.

The dimensions of the level ice sheet are given in Table 13.

Definitions	**Symbols**	**Values**	**Units**
Ice cover size	LxL	100x100	m^2
Ice thickness	h_i	1.0	m
Freeboard	w_f	0.1	m

Table 13: Geometrical parameters of the level ice sheet.

Table 14 lists the DEM analysis for the ice material. The boundary conditions set to the ice sheet are defined in order to simulate an infinite domain and, therefore, the motion of the particles at the sides are constraint in the Y direction, as well as all the three angular rotations.

Definitions	Symbols	Values	Units
Type of ice	-	Level ice	-
Ice velocity	v_i	0.0	m/s
Density of sea ice	ρ_i	920	kg/m^3
Young Modulus of sea ice	E	1e+9	Pa
Poisson ratio of sea ice	ν	0.33	-
Friction angle of sea ice	ϕ_i	30	^{o}
Ice-ice (static) friction	μ_{ii}	0.05	-
Ice-structure (static) friction	μ_{is}	0.25	-
Normal tensile strength	σ_t^f	1.5	MPa
Shear strength	τ^f	1.0	MPa

Table 14: DEM analysis for the level ice material.

In Table 15 the numerical parameters for the Tor Viking II ice-breaking ship are listed.

Definitions	Symbols	Values	Units
Type of structure	-	Ice-breaking ship	-
Cruising velocity	v_s	5.14 (10)	m/s (kn)
Young Modulus	E_s	200e+9	Pa
Poisson ratio	ν_s	0.265	-
Max. Power	P	13440 (18300)	kW (HP)

Table 15: Computational parameters for the Tor Viking II icebreaker ship.

Finally, the DEM simulation parameters are listed in Table 16.

Definitions	Symbols	Values	Units
Mesh packing	-	Unstructured	-
DE type	-	Spheres	-
DE diameter	d_s	0.25 (4 layers)	m
# of DE	N_p	556913	-
Time step	Δt	3.0e-5	s
Total simulation time	T_t	16	s
Calculation time	-	5.89 (16 CPUs)	days

Table 16: DEM parameters for the Tor Viking II ice-breaking ship simulation.

Figure 31 shows the contact failure map at the end of the simulation. Two important conclusions can be drawn:

- The boundary conditions at the sides emulating infinite extension are working efficiently, as ice only influences the ship trajectory. The grey particles are the ones which do not fail, whereas the ones in blue are the broken particles.

- Non radial cracks in the ice sheet plane appear, which is the observed behavior in the field. Only at the end of the simulation, two radial cracks appear due to the influence of the end boundary.

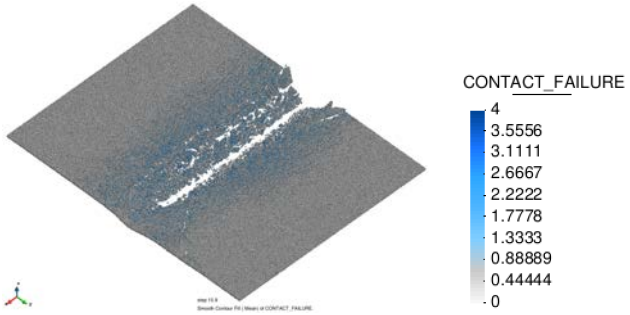

(a) Isometric view. (b)

Figure 31: Failure produced in the ice sheet at the end of the simulation. Tension and shear failure is represented by values 4 and 2, respectively in the colour table

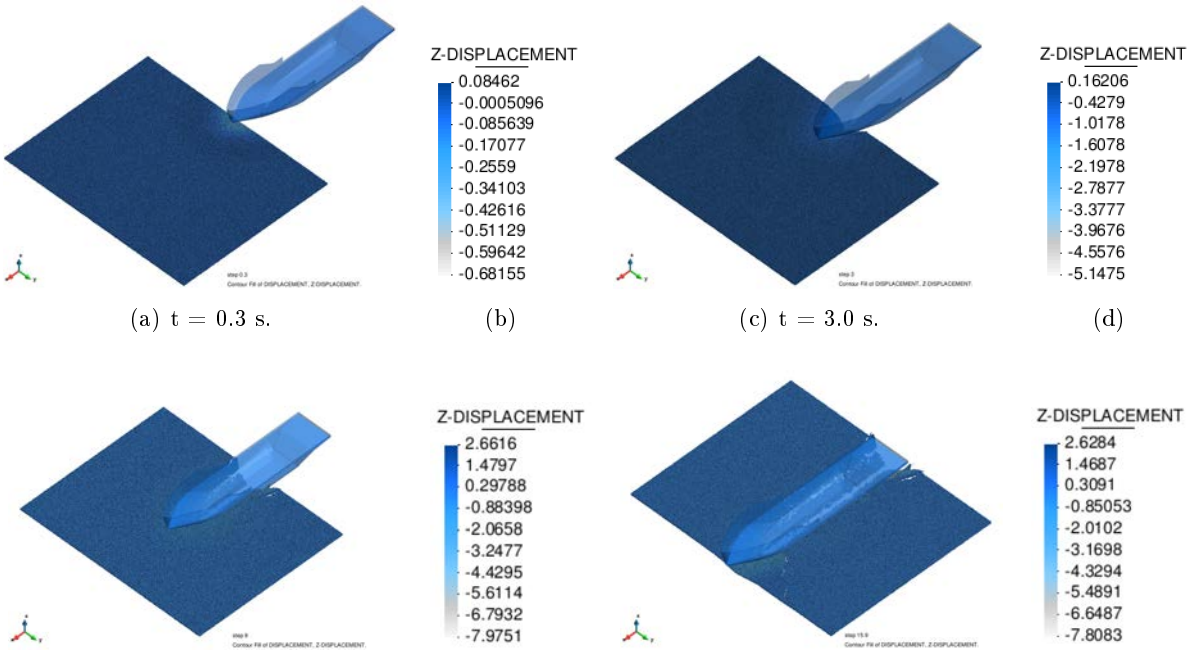

(a) t = 0.3 s. (b) (c) t = 3.0 s. (d)

(e) t = 9.0 s. (f) (g) t = 15.9 s. (h)

Figure 32: Interaction between the Tor Viking II ice-breaking ship and an infinite level ice sheet simulated with the DEM. The magnitude of the Z-displacement is presented.

Figure 32 shows the evolution at different time steps of the simulation with interaction between the Tor Viking II ice-breaking ship and an infinite level ice sheet of 1.0 m thickness and 100x100 m^2.

Observation of the simulation results highlight that when an icebreaker navigates through a continuous ice platform it needs to break the ice to advance, but only failure is produced around the ship. The local out-of-plane bending failure is the most important one, which is continuously induced when the ship advances. The ship breaks and creates its own path generating small ice pieces, as already shown in Figure 2b.

At the beginning of the simulation, when the ice-breaking ship encounters the level ice platform for the first time, some crushing is produced. This crushing, however, has little effect in the overall breaking of the ice sheet.

The broken pieces are submerged up to at most -9.0 m. For longer simulation times the

broken ice pieces experience the buoyancy effect and travel up to the sea surface, creating a channel behind the ship path and formed by brash ice.

Figures 33, 34 and 35 show, respectively, the evolution of the X-, Y- and Z-component of the ice load. As in previous examples, data has been smoothed by taking the median over a window of 100 data points.

The smoothed values fluctuate between 2821.1 kN (max.) to 0 kN (min.) for the X direction, between 1336.7 kN (max.) to -922.5 kN (min.) and 3052.1 kN (max.) to 0 kN (min.).

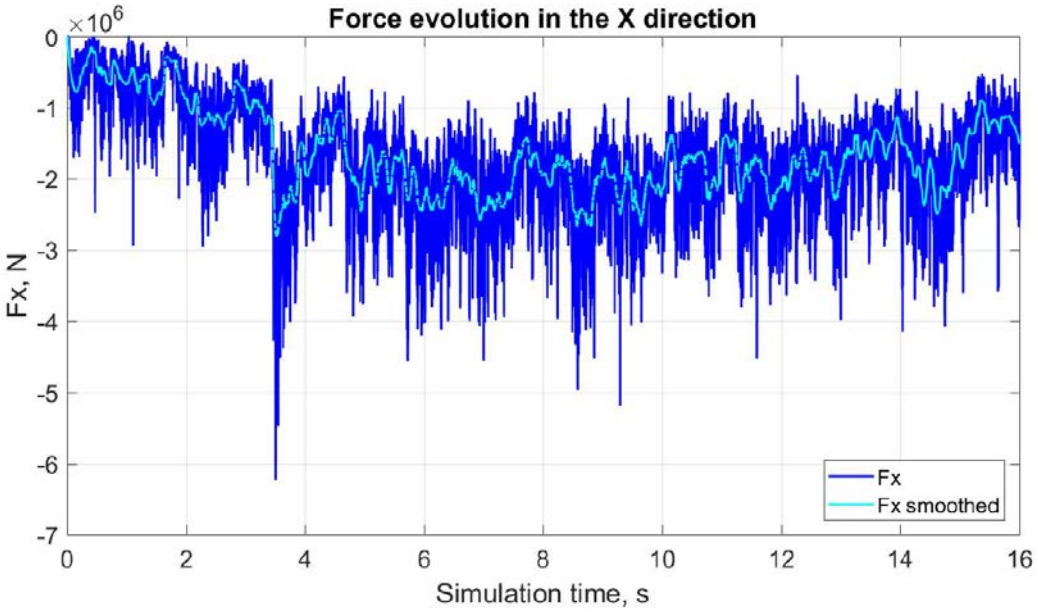

Figure 33: Tor Viking II simulation. Ice force evolution in the X direction.

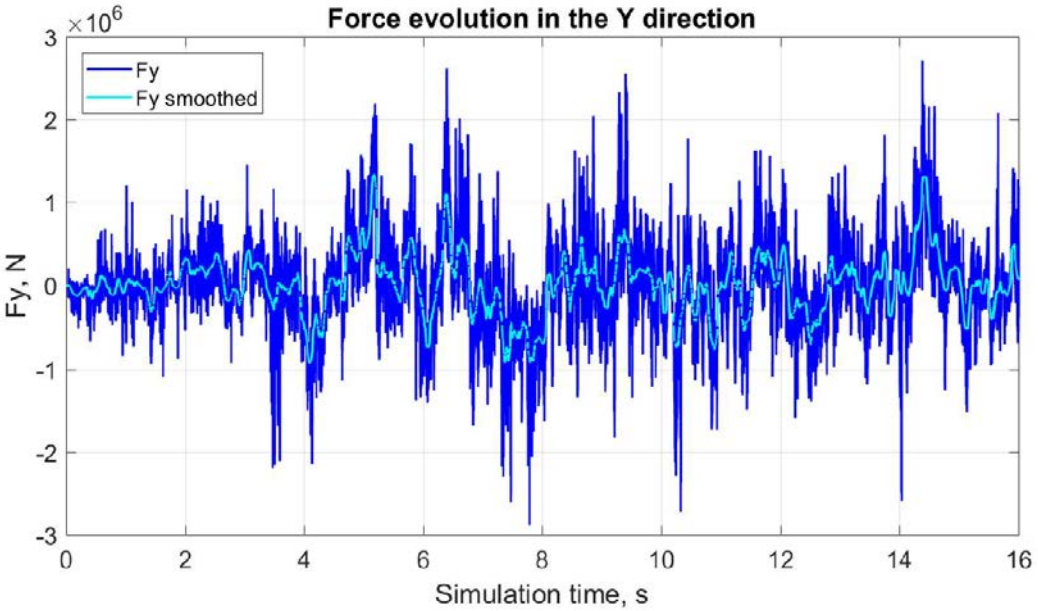

Figure 34: Tor Viking II simulation. Ice force evolution in the Y direction.

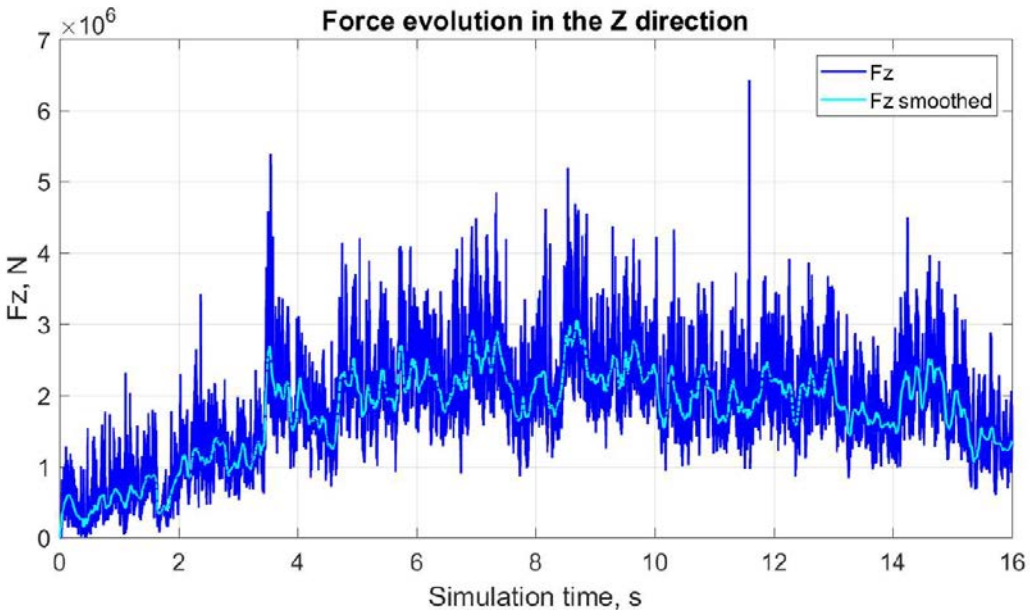

Figure 35: Tor Viking II simulation. Ice force evolution in the Z direction.

The Y-component is the smaller one. This can be related in some way to the absence of in-plane fractures. However, the X- and Z-components have more or less the same values, between 1500 kN to 2500 kN.

From an engineering point of view, the more relevant ice loads are the maximum horizontal and vertical components. From these forces, further studies and conclusions can be drawn in terms of ship power and ship design criteria.

$\mathbf{F}_{x_{max}}$		$\mathbf{F}_{y_{max}}$		$\mathbf{F}_{z_{max}}$	
2821.1	kN	1336.7	kN	3052.1	kN

Table 17: Tor Viking II simulation. Maximum ice loads in the X, Y & Z directions.

If the axial ice loads range from 1500 kN to 2500 kN, taking 2500 kN, the associated propulsion power is 12850 kW (notice that v = 5.14 m/s). This power is slightly smaller than the maximum one for the Tor Viking II icebreaker ship (13440 kW). We consider this a reasonable result as this ship is able to navigate at most in 1.0 m thick ice.

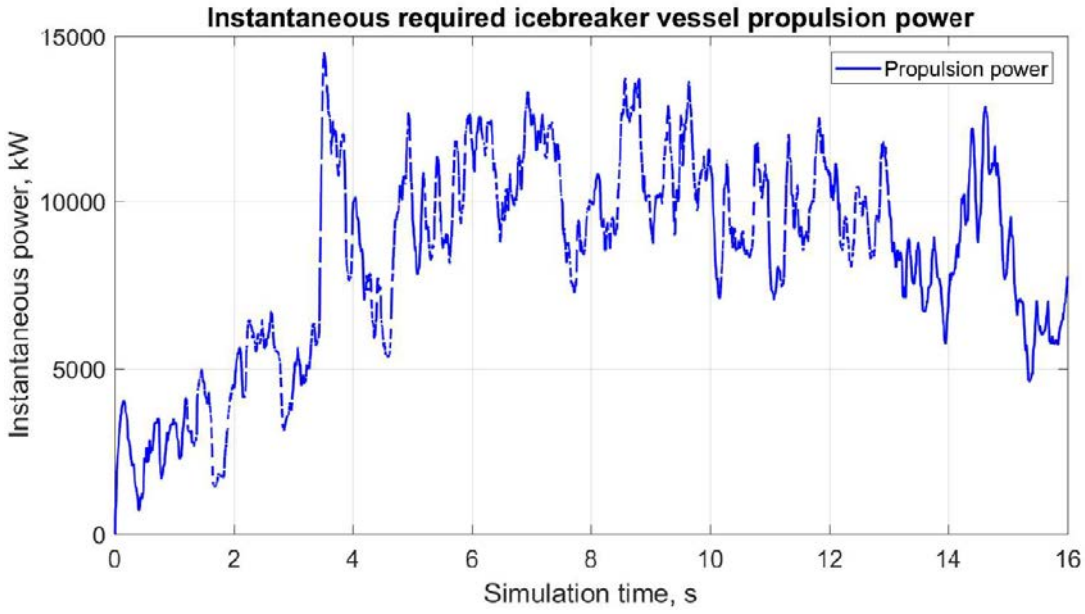

Figure 36: Tor Viking II simulation. Estimated propulsion power evolution.

7 Conclusions

The following list summaries the most relevant aspects regarding the bonded DEM simulations of ice-ship interaction problems carried out in this work:

- In the first group of simulations we have been studied the influence of the slope angle of a cone interacting with an ice sheet in the type of ice fractures and the magnitude of the ice loads. The flatter is the slope, bending dominates, no crushing occurs and lower are the ice loads.

- The upper-lower cone simulations have been used to validate the local bonded DEM for modeling ice fracture. The bonded DEM results are in good agreement with other simulations reported the literature.

- In the second group of simulations we have studied the influence of ice thickness, floe size and ice confinement in the type of failure of a finite size ice floe, and the magnitude of the induced ice loads when ice is loaded by an idealized icebreaker ship bow.

- In general, ice loads increase as ice thickness and ice dimensions do. Also, with the navigation speed considered, the propulsion power computed is low. This explains why a larger number of ships can navigate through broken ice.

- In the third group of simulations we have studied the performance of the Tor Viking II icebreaker ship when navigating through a continuous sheet of level ice. The out-of-plane bending is well reproduced and dominates the failure pattern. Radial cracks do not appear due to the side confinement of the ice sheet.

- Assuming that the motion of the ship bow is kept constant, results show that this icebreaker ship is capable to cruise according to its maximum propulsion power capacity when navigating through a level ice sheet of one meter thick. The computed propulsion power agrees with its theoretical capacity.

As a general conclusion, we have shown that the local bonded DEM developed in [31] is capable of capturing complex ice fracture phenomena during ice-ship interaction situations. The bonded DEM is therefore a promising numerical technique for investigating the behavior and fracture of sea ice and the performance of icebreaker ships and other vessels cruising in icy sea environments, and the mechanical behavior of marine structures under loads induced by ice.

8 Acknowledgments

This research was supported by the NICESHIP project of the Office of Naval Research Global under Navy Grant N62909-16-1-2236 and the ICEBREAKER Proof of Concept project of the European Research Council.

Conflict of Interest

On behalf of all authors, the corresponding author states that there is no conflict of interest.

References

[1] Barber, B.H., Baez, L.M. and North, G.J. (1975). Structural considerations in the design of the POLAR Class of Coast Guard icebreakers. New York, N.Y., USA. The Society of Naval Architects and Marine Engineers.

[2] Celigueta, M.A., Latorre, S., Arrufat, F. and Oñate, E. (2017). Accurate modelling of the elastic behavior of a continuum with the Discrete Element Method. Journal of Computational Mechanics, 60 (6), 997-1010.

[3] Celigueta M.A., Latorre, S., Arrufat F., Oñate E. (2019). An accurate non-local bonded discrete element method for non linear analysis of solids. Application to concrete facture. Computational Particle Mechanics (Submitted)

[4] Cundall P.A., Strack O.D.L. (1979) A discrete numerical model for granular assemblies. Geotechnique 29(1):47–65

[5] Di, S., Xue, Y., Wang, Q. and Bai, X. (2017). Discrete element simulation of ice loads on narrow conical structures. Journal of Ocean Engineering. 146, 283-297.

[6] Det Norske Veritas (DNV), 2003. Ships for navigation in ice. Norway.

[7] Donzé F., Richefeu F., Magnier S. (2009). Advances in Discrete Element Method applied to soil, rock and concrete mechanics. Electronic Journal of Geotechology Engineering 8:1âĂŞ44

[8] Feng Y.T., Han K., Owen D.R.J. (2004). Discrete element simulation of the dynamics of high energy planetary ball milling processes. Materials Science and Engineering A 375:815–819

[9] Government of Canada (2012). Ice navigation in Canadian waters. Ottawa, Ontario. K1A 0E6.

[10] Horner D.A., Peters, F.J., Carrillo A. (2001). Large scale discrete element modeling of vehicle-soil interaction. Journal of Engineering Mechanics 127(10):1027–1032

[11] Høyland, K.V. (2017). Compendium part I, Ice and Arctic - TBA4265 Arctic and Marine Civil Engineering. *Norwegian University of Science and Technology, Trondheim, Norway.*

[12] ISO 19906 (2010). Petroleum and natural gas industries. Arctic offshore structures. International Standard. *Industries du pétrole et du gaz naturel - Structures arctiques en mér*, Geneva, Switzeland.

[13] Ji, S., Di, S. and Liu, S. (2015). Analysis of ice load on conical structure with Discrete Element Method. Int. Journal for Computer-Aided Engineering and Software, 32 (4),1121-1134.

[14] Jia, Z., Ulfvarson, A., Ringsberg, J.W., et al. (2009). A return period based plastic design approach for ice loaded side-shell/bow structures. Journal of Marine Structures. 22 (3), 438-456.

[15] Jou, O., Celigueta, M.A. and Oñate, E. (2018). Theoretical study about sea ice behaviour, analysis of floe-ice fractures and discrete element modelling for ship-ice interactions. *Universitat Politecnica de Catalunya, Barcelona, España*, Master's Degree thesis.

[16] Kim, M.C., Lee, S.K., Lee, W.J., et al. (2013). Numerical and experimental investigation of the resistance performance of an ice-breaking cargo vessel in pack ice conditions. Int. Journal of Naval Architecture. Ocean Engineering. 5 (1), 116-131.

[17] Kuehn, G.A., Lee, R.W., Nixon, W.A. and Schulson, E.M. (1990). The structure and tensile behaviour of first-year sea ice and laboratory-grown saline ice. Journal of Offshore Mechanics and Arctic Engineering, 112, 357-363.

[18] Kujala, P. (1991). Damage Statistics of Ice-strengthened Ships in the Baltic Sea 1984-1987. Winter Navigation Research Board:Finnish Board of Navigation and Swedish Administration of Shipping and Navigation. Technical Report No 50. Espoo, Finland.

[19] Kwok, R. and Cunningham, G.F. (2012). Deformation of the Arctic Ocean ice cover after the 2007 record minimum in summer ice extent. Journal of Cold Regions Science and Technology. 69 (1), 17-23.

[20] Labra C., Oñate E. (2009). High-density sphere packing for discrete element method simulations. Commun Numer Meth Engng 25(7):837–849

[21] Labra C., Rojek J., Oñate E., Zárate F. (2008). Advances in discrete element modelling of underground excavations. Acta Geotechnica 3(4):317–322

[22] Lade, P.V. (2002). Characterization of the mechanical behavior of sea ice as a frictional material. Journal of Geophysical Research, 107(B12), 23-77.

[23] Løset, S., Shkhinek, K. N., Gudmestad, O. T. and Høyland, K. V. (2006). Actions from ice on Arctic offshore and coastal structures. St. Petersburg: LAN.

[24] Lu, W. (2014). Floe ice-sloping structure interactions. *Norwegian University of Science and Technology, Trondheim, Norway*, Philosophiae Doctor Degree thesis.

[25] Lu, W., Løset, S. and Lubbad, R. (2012). Simulating ice-sloping structure interactions with the Cohesive Element Method. *Proceedings of the ASME 2012 31st Int. Conference on Ocean, Offshore and Arctic Engineering, Rio de Janeiro, Brasil.*

[26] Lubbad, R. and Løset, S. (2011). A numerical model for real-time simulation of ship-ice interaction. Journal of Cold Regions Science and Technology, 65, 111-127.

[27] Lu, W., Lubbad, R. and Løset, S. (2014). In-plane fracture of an ice floe: A theoretical study on the splitting failure mode. Journal of Cold Regions Science and Technology. 110, 77-101.

[28] Lu, W., Lubbad, R. and Løset, S. (2015). Out-of-plane failure of an ice floe: Radial-crack-initiation-controlled fracture. Journal of Cold Regions Science and Technology. 119, 183-203.

[29] Lu, W., Lubbad, R., Løset, S. and Kashafutdinov, M. (2015). Fracture of an ice floe: Local out-of-plane flexural failures versus global in-plane splitting failure. Journal of Cold Regions Science and Technology. 123, 1-13.

[30] Oñate, E. and Rojek, J. (2004). Combination of discrete element and finite element method for analysis of geomechanics problems. Comput. Methods Appl. Mech. Eng. 193, 3087-3128.

[31] Oñate E., Zárate F., Miquel J., Santasusana M., Celigueta M.A., Arrufat F., Gandikota R., Valiullin K., Ring L. (2015). A local constitutive model for the discrete element method. application to geomaterials and concrete. Computational Particle Mechanics 2:139–160

[32] Paavilainen, J., Tuhkuri, J. and Polojärvi, A. (2011). 2D numerical simulations of ice rubble formation process against an inclined structure. Journal of Cold Regions Science and Technology. 68, 20-34.

[33] Polojärvi, A. and Tuhkuri, J, (2009). 3D discrete numerical modelling of ridge keel punch through tests. Journal of Cold Regions Science and Technology. 56, 18-29.

[34] Potyondy D., Cundall P. (2004). A bonded-particle model for rock. International Journal of Rock Mechanics and Mining Sciences 41(8):1329–1364

[35] Rojek J., Labra C., Su O., Oñate E. (2012). Comparative study of different discrete element models and evaluation of equivalent micromechanical parameters. Int J of Solids and Structures 49:1497–1517

[36] Schulson, E.M. (1999). The structure and mechanical behaviour of ice. Journal of the Minerals, Metals and Materials Society.

[37] Schulson, E.M. (2001). Brittle failure of ice. Journal of Engineering Fracture Mechanics, 68 (1), 1839-1887.

[38] Schulson, E.M. (2006). The fracture of water ice Ih: A short overview. Journal of Meteoritics and Planetary Science, 41(10), 1497-1508.

[39] Sun, S.S., Shen, H.H. (2012). Simulation of pancake ice load on a circular cylinder in a wave and current field. Journal of Cold Regions Science and Technology. 78, 31-39.

[40] Tatinclaux, J.C.P. (1988). Ship model testing in level ice. US Army Corps of Engineers.

[41] Timco, G.W. and Weeks, W.F. (2010). A review of the engineering properties of sea ice. Journal of Cold Regions Science and Technology. 60 (1), 107-129.

[42] Tran V.T., Donzé F.-V., Marin P. (2011). A discrete element model of concrete under high triaxial loading. Cement and Concrete Composites 33(9):936âĂŞ948

[43] USCG Office of Waterways and Ocean Policy (CG-WWM) (2017). Chart of the major icebreakers of the world.